Applied Surface Science 629 (2023) 156502

Contents lists available at ScienceDirect

Applied Surface Science

journal homepage: www.elsevier.com/locate/apsusc

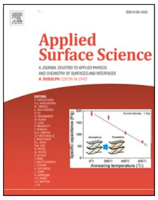

Full Length Article

Probing the molecular-level energy absorption mechanism and strategic sequencing of graphene/*Al* composite laminates under high-velocity ballistic impact of nano-projectiles

K.K. Gupta [a], T. Mukhopadhyay [b,*], S. Dey [a]

[a] *Department of Mechanical Engineering, National Institute of Technology Silchar, Silchar, India*
[b] *Faculty of Engineering and Physical Sciences, University of Southampton, Southampton, UK*

ARTICLE INFO

Keywords:
Kinetic energy absorption
High-velocityimpact
Ballistic performance of graphene/Al composites
Graphene reinforced aluminum composite
Disordered graphene composites

ABSTRACT

Motivated by recent discoveries concerning the extreme superiority of multilayer graphene in terms of kinetic energy dissipation compared to conventional monolithic materials, this article investigates the ballistic performance and physics-informed strategic sequencing of graphene-reinforced aluminum laminates under the influence of random disorder based on extensive molecular-level simulations of high-velocity impact. It is unraveled that strategic sequencing of graphene layers within the aluminum matrix can significantly enhance kinetic energy absorption, while preventing complete penetration. However, the reinforcement of bilayer graphene increases the projectile's post-impact residual velocity due to high magnitude of stress wave release provided by the reinforcement. We have further mitigated this effect to a significant extent by increasing the effective thickness of *Al* laminates. Based on the insights gained by a series of molecular-level simulations, we have proposed hybrid multifunctional laminates by coupling two individual configurations with high energy absorption and no penetration, respectively. By strategically providing higher graphene concentration near target surfaces, up to 90.77% of the kinetic energy can be absorbed. The findings of this study would be crucially useful in materializing the bottom-up multi-scale design pathway for producing graphene-reinforced *Al* composites to develop a novel class of functional barrier material-based engineered surfaces with improved nano-scale ballistic performance.

1. Introduction

The quest for lightweight armor materials has inspired the scientific community to explore the novel class of graphene-based composites for achieving high specific energy absorption capability [1-5]. Such materials can be used in a variety of applications, including the development of lightweight body armors for military personnel [6], bulletproof automotive structures [7], aerospace and flight structures [8], and materials for turbine blades to resist shock loading caused by supersonic particle impact [9]. The extraordinary mechanical behavior of graphene can be harnessed to develop multifunctional composites having high penetration resistance and energy absorption.capabilities along with other mechanical properties related to specific strength and stiffness. Being one of the lightest (density $\approx 0.77\ \mathrm{mgm}^{-2}$), stiffest ($Y \approx 1$ TPa), and strongest (fracture strength ≈ 130 GPa) materials, graphene as the reinforcement material can result in composite structures with exceptional strength to weight ratio. Recent laser-induced micro-projectile tests on multilayer graphene (MLG) have revealed its extreme superiority in terms of kinetic energy dissipation compared to conventional monolithic materials like steel, with the specific penetration energy offered by the MLG being in the order of $1\ \mathrm{MJ\,kg}^{-1}$ [10]. This establishes a strong rationale for exploring the dynamic behavior of graphene-based metal matrix composites subjected to ballistic impact loading for further performance enhancement. In this paper, we would present the ballistic performance and physics-informed strategic sequencing of graphene-reinforced aluminum laminates under the influence of random disorder based on extensive molecular-level simulations of high-velocity oblique impact.

For several years, the multi-physical properties of graphene and its derivatives [11-13,64] have piqued the interest of the research community. The mechanical and structural characteristics of such nanomaterials are extensively explored using experimental and

---

[*] Corresponding author.
E-mail address: t.mukhopadhyay@soton.ac.uk (T. Mukhopadhyay).

https://doi.org/10.1016/j.apsusc.2023.156502
Received 3 October 2022; Received in revised form 31 December 2022; Accepted 17 January 2023

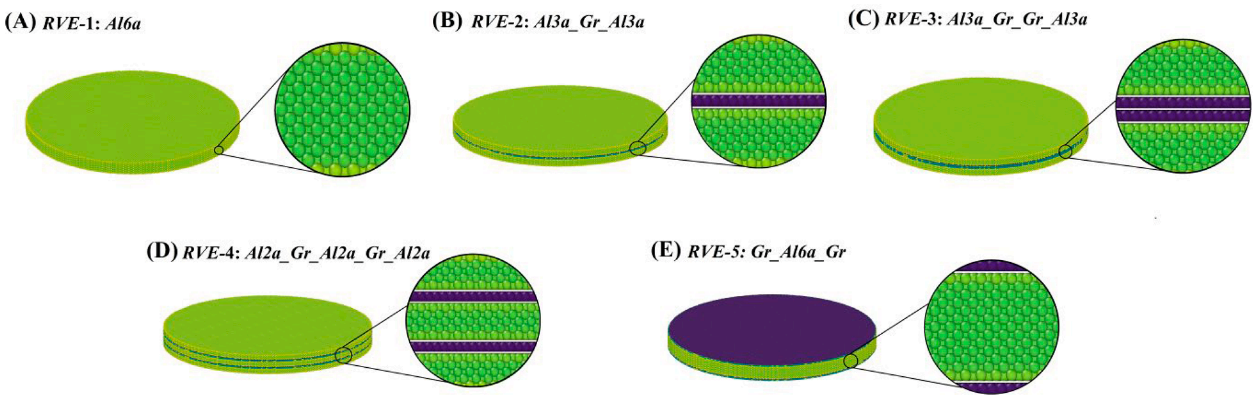

Fig. 1. Atomistic models of *Al* laminate and its graphene reinforced *RVE*s. (A) *RVE*-1:Pure *Al* laminate with the thickness of 6*a* (B) *RVE*-2: *Al* laminate (thickness 6*a*) reinforced with single-layer graphene in the sequence of *Al3a*-graphene-*Al3a* (C) *RVE*-3: *Al* laminate (thickness 6*a*) reinforced with bilayer graphene in the sequence of *Al3a*-graphene-graphene-*Al3a* (D) *RVE*-4: *Al* laminate (thickness 6*a*) reinforced with two single-layer graphenes distributed in the sequence of *Al2a*-graphene-*Al2a*-graphene-*Al2a* (E) *RVE*-5: *Al* laminate coated by single-layer graphene on both the faces in the sequence of graphene-*Al6a*-graphene. In all the *RVE*s, the effective thickness of *Al* laminates is described as a multiple of *a*, where *a* is the lattice constant of *Al*.

computational methods [14-19]. The superior mechanical strength of the graphene and its derivatives is expected to improve the strength of its metal matrix composites by many-fold [20-22], which is generally not evident in the graphene-based metal matrix composites. Such a decline in the expected mechanical strength of graphene-reinforced metal matrix composite can be associated with the formation of multiple inherent structural challenges, such as weak interfacial interaction between graphene and metal [23], formation of metal carbide [24], and agglomeration of graphene flakes due to the presence of van der Waals forces [25]. The recent efforts of a few research groups have paved the novel ways to produce graphene reinforced metal matrix composite with higher strength and minimized structural irregularities. For example, Dixit *et al.* [26] reported a two-fold increase in the strength of graphene-reinforced aluminum composites produced by friction stir alloying, whereas Zhang *et al.* [27] produced the high strength graphene reinforced aluminum composites by reduction of graphene oxide using the powder metallurgy technique. In another study, Xie *et al.* [28] reported that the deformation-driven metallurgy results in high-performance graphene reinforced aluminum composites with ultrafine microstructures. To reduce the challenges associated with a uniform dispersion of graphene in the metal matrix composites, Zhang *et al.* [29] integrated the powder metallurgy with friction stir processing to retain the layered structure of graphene within the aluminum-based composites. Such recent efforts in producing the high-strength metal matrix composites of graphene have created a strong rationale to explore the multi-faceted properties of such composite structures, which will open new avenues in the development of application-specific multi-functional materials. Since the prospective performance of graphene based metallic composites has not been adequately explored despite promising capabilities in terms of other mechanical properties with the advancement in manufacturing, we aim to focus on the ballistics of graphene/ *Al* composites including various practically-relevant manufacturing conditions.

As the failure of any material system initiates at the atomic scale, molecular dynamics (MD) simulations can be one of the most reasonable ways to characterize the nanoscale behavior of a material. The MD simulations have been utilized to successfully characterize different stages of metal crystallization [30,31]. Moreover, graphene and its derivatives being nanoscale materials have been explored extensively by performing MD simulations [32-36,60]. In recent years, MD simulation has also been used to characterize the ballistic performance of graphene and other 2D materials [37-39]. Various polymer/metal/ceramic based thin-film structures are also characterized for their superior ballistic performance using MD simulations [40-44]. To scale up the material discovery, the efforts of integrating graphene with the metal and ceramic matrix have been made by utilizing material modeling and performing atomistic simulations [45-49]. The nanoscale investigation of the ballistic performance of graphene reinforced aluminum structure is scarce to find in the literature. The ultrasonic pulse-driven targeted penetration of tissues performed by using micro cannons further establishes the need to understand the impact performance of materials on the nanoscale [50]. The recent laser-induced micro-projectile impact tests have led to proposing a few promising barrier materials [10,62,63]. However, such experiments possess the limitation of not unveiling the mechanism of kinetic energy dissipation at the fundamental atomic level. A few research groups reported the ballistic performance of graphene-reinforced/coated metal and ceramic composites by utilizing MD simulation. For instance, Wu *et al.* [51] demonstrated the self-healing process of the impacted graphene/*Cu* interface by conducting MD simulation of high-velocity impact on the single layer graphene reinforced copper laminate. In another study, Tian and Zhang [45] reported an enhancement in the surface hardness of *SiC* laminate by coating it with single and multi-layer graphene films. They conducted MD simulations of nano-indentation and high-velocity impact to analyze the superior dynamic response of graphene-coated *SiC* laminates. Motivated by promising results from the literature, in the present analysis, we focus on the ballistic performance of graphene/*Al* laminates. A detailed analysis of the present article would elucidate the mechanism of kinetic energy dissipation and dynamic failure of graphene/*Al* thin film laminates at the atomic scale. The scientific contribution of this article is to explore the influence of the stacking sequence of graphene reinforcements on the ballistic performance of graphene/*Al* thin film laminates under the high-velocity impact of nano-projectiles. In this regard, we would present extensive MD simulations based on representative volume elements (*RVE*s) to ascertain the mechanism of kinetic energy absorption exhibited by different stacking sequences of graphene and *Al* laminates. Thereby we aim to identify the most favorable stacking sequence of graphene/*Al* laminates for maximizing ballistic performance. Along with the kinetic energy dissipation, the impact performance of the considered *RVE* models would also be assessed by the extent of deflection/damage caused by high-speed nano-projectiles. Such nano-engineered materials can find their applications in the development of armor materials against high-velocity impact. Hereafter, the paper is organized as: section 2 provides all necessary details for modeling the different *RVE*s and performing the MD simulations, section 3 presents the interpretation of numerical results gathered by a series of MD simulations, and finally, the conclusion of the study is provided in section 4.

Table 1
Energy and distance parameters for the non-bonded *LJ* interactions between the atoms.

Atoms	ε (eV)	σ (Å)
Al-Al [23]	0.392	2.620
C–C [34,39]	0.00285	3.4
Al-C [56]	0.03507	3.0135

2. Modeling and simulations

The details of modeling various graphene-reinforced aluminum laminates (*RVE*s) and then exposing these structures to high-velocity impact (with varying velocity) are explained in this section. The *RVE*s are modeled by varying the stacking sequence of the constituent graphene and aluminum laminates (as shown in Fig. 1). The thickness of the *Al* laminates is measured in multiples of the lattice constant ($a = 4.05$ Å). For example, *RVE*-1 (*Al6a*) refers to an *Al* laminate with a thickness of 24.3 Å ($6a = 6 \times 4.05$ Å), whereas other *RVE*s are modeled by splitting *Al6a* into two laminae of *Al3a* (for *RVE*-2 and *RVE*-3) and three laminae of *Al2a* (for *RVE*-4), with graphene reinforced in between the *Al* layers, as shown in Fig. 1(B-D). The *RVE*-5 is modeled by coating the *Al6a* with a graphene layer on the target face and rear face of the structure as shown in Fig. 1(E). Following a similar procedure the other *RVE*s (*RVE*-(6–10)) used in the later part of the study are modeled (refer to Fig. 12).

We have maintained the same radii of the target structures as 215 Å while the targets are clamped at the edges up to the width of the 15 Å; hence the effective radii (R) of the targets are maintained at 200 Å throughout the study. The targets are impacted by cylindrical projectiles (made of gold), and the height (h) and radius (r) of the projectile are maintained at 78 Å and 28 Å throughout the study. It is noteworthy to mention that the ratio of the effective radius of the target and the projectile (R/r) is maintained as more than 5 (≈7.1) to avoid the boundary effects [52]. The modeling of *Al* laminates, monolayer, and bilayer graphene is carried out by using the open-source tool *VESTA* [53], whereas different *RVE*s are prepared by packing the graphene and *Al* laminates together in different stacking sequences by employing another open-source code *packmol* [54]. The equilibrium interlayer distance between graphene and *Al* is reported in the range of 2.31–3.36 Å by the observations gathered from the experiments and first-principle calculations [55]; in the present study, we have modeled the graphene and *Al* laminates with the interlayer distance of 3.014 Å [56]. The interlayer distance between individual layers of the bilayer graphene is kept as 3.4 Å [34,39]. The interatomic interactions between aluminum atoms within the *Al* laminates are modeled by the modified embedded-atom method (*MEAM*) force-field [57]; likewise, the interactions between gold atoms within the projectile are modeled by the *MEAM* force field. The interatomic interactions between carbon atoms within the graphene layer are modeled by employing the *AIREBO-m* force field [58], wherein the Lennard-Jones potential in the conventional *AIREBO* force field is replaced by *Morse* potential to correctly mimic the high-pressure deformation and breaking of bonds [59]. The non-bonded interlayer interactions within the *Al-Al, C–C,* and *C-Al* atoms are captured by the *Lennard-Jones* (*LJ*) forcefield, wherein the relevant energy, and distance parameters of the *LJ* force field are provided in Table 1.

The MD simulations of the high-velocity impact are conducted in the *LAMMPS* [60] environment, where the simulation box is enforced with periodic boundary conditions in the x and y directions. The iteration timestep is used as 0.1 fs (femtoseconds). In the initial stage of the simulation, at first, the potential energy of the structure is minimized by using a conjugate gradient minimization algorithm where the energy tolerance and force tolerance are used as 1×10^{-10} (unitless quantity) and 1×10^{-4} eV/Å^3, respectively. The process of energy minimization is performed for 5 ps (picoseconds). In the next step, the pressure and temperature equilibration of the energy-minimized structure is performed under the isothermal-isobaric (NPT) ensemble to maintain the structure at a temperature of 300 K and eliminate the residual stresses in the structure. The equilibration is performed for 10 ps. The relaxed structure is then impacted with the rigid cylindrical projectile under the NVE ensemble at different impact velocities. The development of the stress distribution in the structure as a consequence of the high-velocity impact is recorded as Von-Mises stress. The impact simulation is performed for 50 ps and atomistic trajectories are observed using the *OVITO* [61]. As a response, the time history of kinetic energy (*KE*) and velocity (V) of the projectile are recorded at each timestep. The difference between the initial kinetic energy and residual kinetic energy of the projectile provides the kinetic energy absorption (E_a) of the structure. The post-impact velocity of the projectile is recorded as the residual velocity (V_r) of the projectile. The time history of the force observed by the projectile while penetration provides the resisting force (F_r) offered by the structure.

Table 2
The comparison of E_p* values with the published literature.

	Impact velocity (m/s)	Aluminum E_p* (MJkg^{-1})	Graphene/ BLG E_p*(MJkg^{-1})
Dewapriya and Miller [44]	500	3.1287	–
	750	3.9825	–
	1000	4.67	–
Present study	500	3.03	–
	750	3.69	–
	1000	4.13	–
Haque *et al.* [59] (Graphene)	5000	–	40.8
Haque *et al.* [59] (BLG)	5000	–	25.2
Present study (Graphene)	5000	–	49.9
Present study (BLG)	5000	–	23.6

3. Results and discussion

In this section, we have presented the numerical results obtained from a series of MD simulations of high-velocity impact on the various configurations of *RVE*s, as discussed in the preceding section. To have adequate confidence in the computational results, we started by validating the specific penetration energy (E_p*) of the *Al* and graphene (separately) with the published literature. The specific penetration energy can be defined as the kinetic energy absorbed by the structure, which is normalized by the mass of the impact zone. The circular *Al6a* (with the thickness 6 times a, where$a$stands for lattice constant of aluminum) sample is modeled with a radius of 215 Å. During the simulation the target is fixed at its edges up to the width of 15 Å; hence, the effective radius of the target is maintained as 200 Å. The *Al6a* target is impacted (with impact velocities of 500 m/s, 750 m/s, and 1000 m/s) with the cylindrical projectile of gold which has a diameter and height of 77 Å and 81 Å, respectively, similar to the study carried out by Dewapriya and Miller [44]. In the case of graphene, the square-sized single layer and bilayer samples are utilized with an edge size of 200 Å. The graphene target is impacted by the C_{180} fullerene projectile with an impact speed of 5000 m/s, similar to a study carried out by Haque *et al.* [59]. The E_p* values obtained from the MD simulations are compared with the published literature, which is presented in Table 2. A good agreement can be found for both the cases of *Al* and graphene (single and bilayer), corroborating the reliability of the computational approach followed in the current study.

3.1. Transverse impact of the projectile

With the adequate confidence corroborated from the validation of specific penetration energies of aluminum and graphene separately, we further carried out extensive MD simulations to ascertain the high-velocity impact resistance of different *RVE*s (which consist of varied stacking sequences of *Al* and graphene; refer to Fig. 1). The radii of

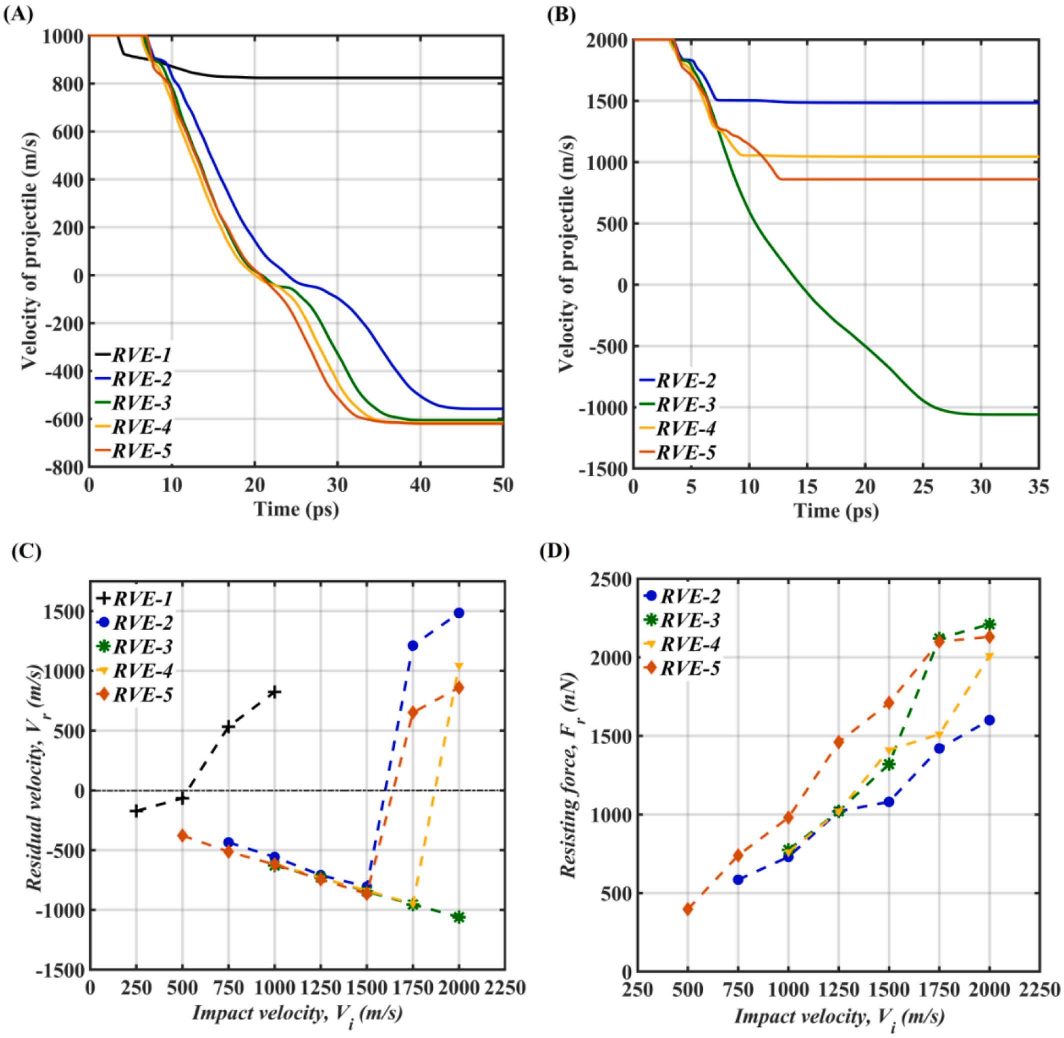

Fig. 2. High-velocity impact responses performed on the considered *RVE*s. (A) Comparison of the timehistory of velocity of projectile for different *RVE*s when impact velocity is 1000 m/s. (B) Comparison of the time-history of velocity of the projectile for different *RVEs* when impact velocity is 2000 m/s. (C) Variation in the residual velocity (V_r) of the projectile for different *RVE*s when impact velocity is varied from 250 m/s to 2000 m/s. (D) Variation in the resisting force (F_r) offered by different *RVE*s when impact velocity is varied from 500 m/s to 2000 m/s.

targets are maintained as 215 Å with the effective radii (R) of 200 Å (fixed edge up to the width of 15 Å). The radius (r) and height (h) of the cylindrical projectile are maintained as 28 Å, and 78 Å, respectively. The post-impact temporal variations in the velocity of the projectile are compared to observe the residual velocity of the projectile. It is observed that the initial impact velocities have a major influence on the residual velocity of the projectile, regardless of the target configurations considered. Fig. 2(A) and 2(B) present a comparison of the variations in the temporal velocities of projectiles with initial impact velocities of 1000 m/s and 2000 m/s, respectively. The sudden drop in the curves denotes the point of impact, and the post-impact asymptotic velocity denotes the projectile's residual velocity. The rebound velocity is represented by the negative post-impact velocity of the projectile, whereas the residual velocity after complete penetration is represented by the positive post-impact velocity of the projectile. It is evident from Fig. 2(A) that at the initial impact velocity of the projectile as 1000 m/s, the *RVE*-1 (pure *Al* laminate with the thickness of 6*a*) demonstrates complete penetration without offering any significant resistance. While the post-impact residual velocities of all the other *RVE*s (from *RVE*-2 to *RVE*-5) can be observed in the negative region (which indicates the rebound of the projectile) when subjected to the impact velocity of 1000 m/s. This indicates that the reinforcement of graphene in the *Al* laminate, wherein the effective thickness of *Al* is maintained at 6*a* (6 times its lattice constant), offers a resistance to the complete penetration of projectile at the velocity of 1000 m/s. The post-impact distribution of von Mises stress in the *RVE*-2 and *RVE*-3 indicates that the single-layer and bilayer graphene, respectively, account for the majority of the stress distribution (visualization provided in supplementary multimedia file MM1; note that the results of both *RVE*-2 and *RVE*-3 are shown in the same frame by showing half of the symmetric domains). It is also observed that at the initial impact velocity of 1000 m/s, the *RVE*-2 (*Al* laminate reinforced with single-layer graphene) offers the least rebound velocity when compared with the *RVE*s reinforced with different sequences of 2 layers of graphene (*RVE*-(3–5)). This can be explained by the higher magnitude of the stress wave release offered by two layers of graphene when compared to its single-layer counterpart (it can be visualized in supplementary multimedia file MM1).

The atomistic snapshots of *RVE*s-(1–5) subjected to the impact velocity of 1000 m/s are illustrated in Fig. 3, which supports the observations gathered from Fig. 2(A). The comparison of the temporal variations in the velocity of the projectile observed in the graphene-reinforced *RVE*s (*RVE*-(2–5)) when the impact velocity is increased to 2000 m/s is illustrated in Fig. 2(B). At the impact velocity of 2000 m/s, apart from *RVE*-3 (*Al* laminate reinforced with the bilayer graphene), all the other *RVE*s demonstrated complete penetration. However, the *RVE*-3 resulted in a very high rebound velocity (nearly half of the impact

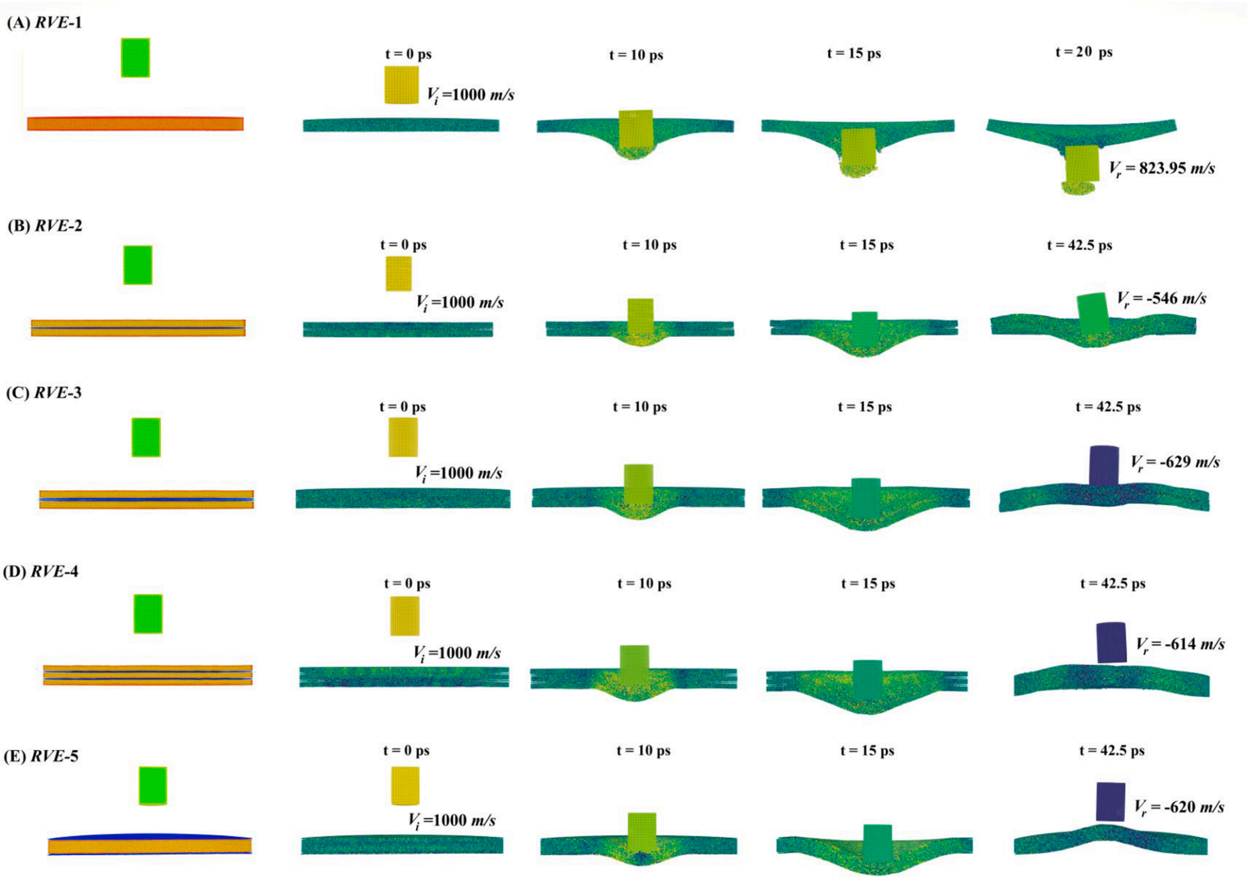

Fig. 3. Trajectories of atomistic model time histories at animpact velocity of 1000 m/s. (A) *RVE*-1 (B) *RVE*-2 (C) *RVE*-3 (D) *RVE*-4 (E) *RVE*-5.

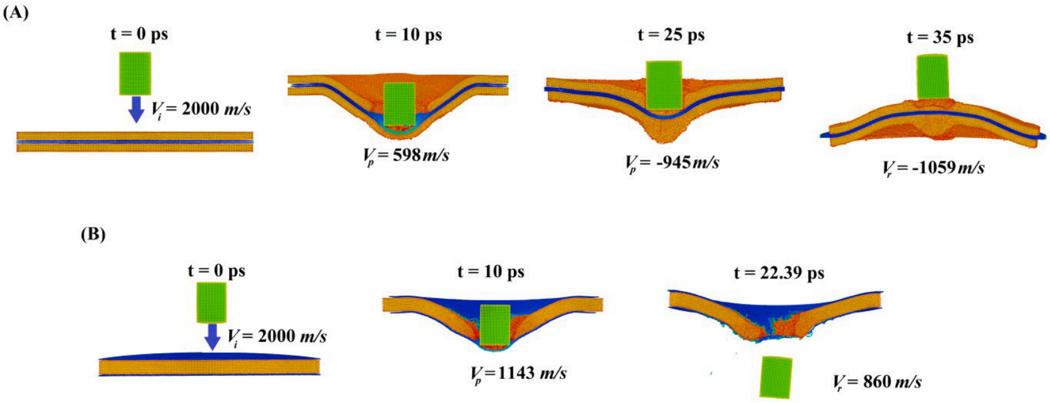

Fig. 4. Comparison of the post-impact performance at the impact velocity of 2000 m/s. (A) *RVE*-3 (B) *RVE*-5.

velocity) of the projectile. The least post-penetration residual velocity of the projectile is offered by the *RVE*-5. Fig. 2(C) depicts the variation in the projectile's residual velocity with respect to the increase in impact velocity for the considered *RVE*s, where the velocity region above zero represents the residual velocity after penetration and the velocity region below zero represents the rebound velocity. Fig. 2(C) shows that *RVE*-1 exhibits the transition from the rebound to complete penetration above the impact velocity of 500 m/s. The graphene reinforced *RVE*s of *Al* laminate, on the other hand, can withstand high-velocity impacts of up to 1500 m/s without penetration. It is also clear that *RVE*-4 and *RVE*-3 can withstand high-velocity impacts of 1750 m/s and 2000 m/s, respectively, without being completely penetrated. It is also observed from Fig. 2(B-C), that *RVE*-3 works better as the reinforcement in terms of penetration resistance when compared with the other *RVE*s, which can be further corroborated by the atomistic snapshots of *RVE*-3 and *RVE*-5 subjected to the impact velocity of 2000 m/s (refer to Fig. 4). It can be noticed that in the cases of graphene-reinforced *RVE*s, the graphene reinforcements dissipate the kinetic energy of the projectile and the residual kinetic energy of the projectile is dissipated by the rebound action (when impact velocity is 1000 m/s). When the impact velocity of the projectile is increased to 2000 m/s, a complete penetration in the *RVE*s occurs except in the case of *RVE*-3, wherein, the reinforcement of bilayer graphene limits the extent of plastic deformation and prevents the complete penetration. However, the elastic deformation of bilayer graphene in the case of *RVE*-3 leads to a relatively higher magnitude of stress wave release, which causes the high rebound velocity (nearly half

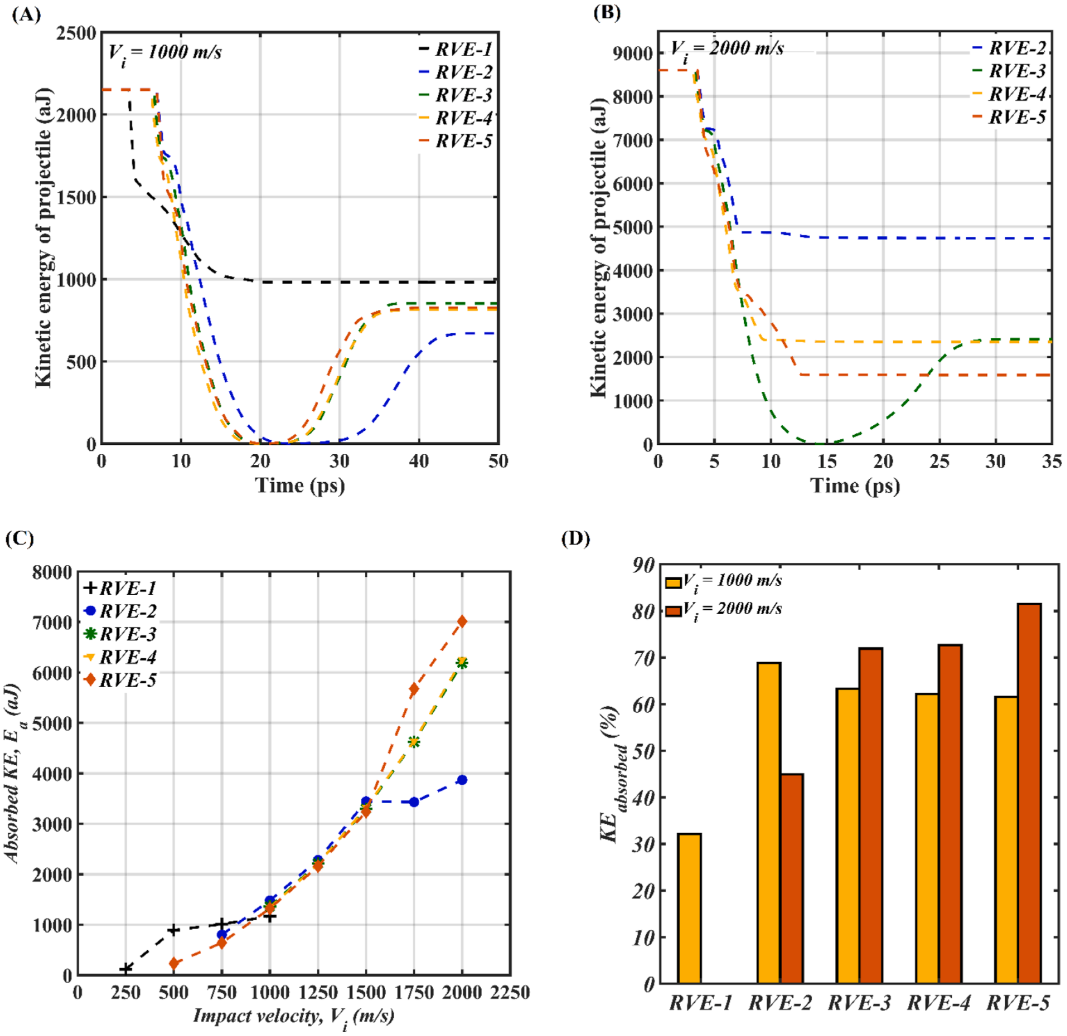

Fig. 5. Kinetic energy absorption capability of the considered *RVE*s. (A) Comparison of the time history of the kinetic energy of projectile for different *RVE*s when impact velocity is 1000 m/s (B) Comparison of the time history of the kinetic energy of projectile for different *RVE*s when impact velocity is 2000 m/s (C) Variation in the kinetic energy absorption (E_a) of the projectile for different *RVE*s when impact velocity is varied from 250 m/s to 2000 m/s (D) Comparison of the percentage of kinetic energy absorbed by the *RVE*s when impacted with the projectile velocity of 1000 m/s and 2000 m/s.

of the impact velocity) of the projectile. The comparison of resisting force offered by the different *RVEs* (to the impacting projectile) at varying impact velocities is illustrated in Fig. 2(D), wherein it can be noticed that the highest resisting force against the impact is offered by the *RVE*-5, regardless of the impact velocity. This can be explained by the direct exposure of the projectile to the graphene at the time of impact. At higher impact velocity (1750 m/s and 2000 m/s) the resisting force offered by *RVE*-3 almost matches with the *RVE*-5. It is worth mentioning that the resisting force is a consequence of immediate indentation resistance offered by the material system at the instance of impact when no bending is involved. Hence, the resisting force does not depend on the film thickness [40].

So far in the preceding paragraphs, we only explained the post-impact residual velocity of the cylindrical projectile for all the *RVE* configurations considered in the study. To ascertain the ballistic performance of the material structure, it is essential to observe how well the kinetic energy is dissipated by the structures. To determine the kinetic energy absorption by the considered structures, the kinetic energy of the projectile is followed for each timestep, from pre-impact to post-impact. The observations corresponding to the kinetic energy absorption of the considered *RVE* configurations are depicted in Fig. 5. Fig. 5(A) depicts the time-history of the projectile's kinetic energy variation when it is subjected to an initial impact velocity of 1000 m/s. The graphene reinforced *RVEs* (*RVE*-(2–5)) exhibit two distinct regimes of kinetic energy variations, wherein at first the kinetic energy of the projectile suddenly reaches zero after the impact and next the projectile again gains the kinetic energy due to stress wave release of graphene reinforcements. This phenomenon is found missing in the *RVE*-1 (which shows the complete penetration at the velocity of 1000 m/s). Similar to the cases of residual velocity illustrated in Fig. 2(A), the *RVE*-2 offers the least post-impact residual kinetic energy at the impact velocity of 1000 m/s. Fig. 5(B) illustrates the time-history of the kinetic energy of the projectile for the graphene-reinforced *RVE* configurations at the impact velocity of 2000 m/s. It can be noticed from the Fig. 5(B) that *RVE*-3 demonstrates similar two distinct regimes of kinetic energy variations as shown by the graphene reinforced *RVEs* at the impact velocity of 1000 m/s, whereas the other *RVEs* offer the kinetic energy transition of the projectile similar to the case of complete penetration (*RVE*-1 in Fig. 5(A)). The least post-impact residual kinetic energy of the projectile is offered by the *RVE*-5; however, the resistance to complete penetration is offered by the *RVE*-3 at the impact velocity of 2000 m/s. The comparison of the magnitude of kinetic energy absorbed by the considered *RVE* configurations at different impact velocities is illustrated in Fig. 5 (C). It is evident from the Fig. 5(C) that up to the impact velocity of 1500 m/s each graphene reinforced *RVEs* (*RVE*-(2–5)) offers almost similar kinetic energy absorption, whereas beyond the impact velocity

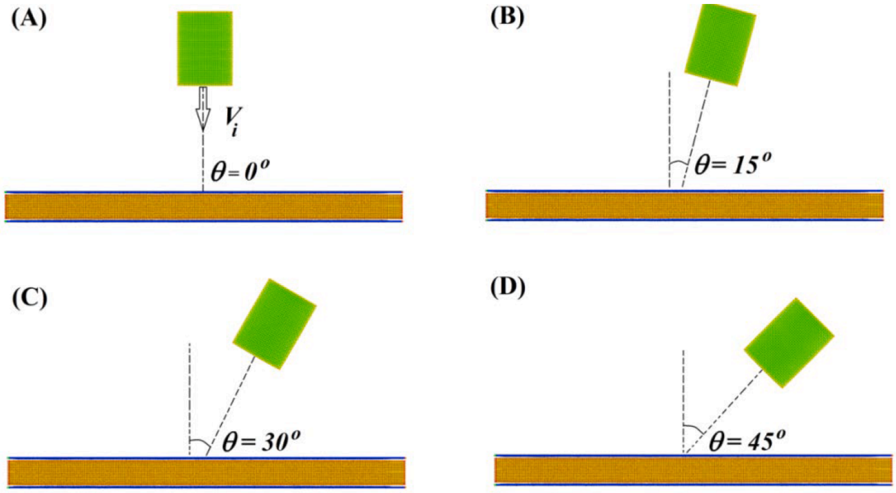

Fig. 6. *RVE*-5 subjected to the oblique impact with an angle of impact considering cylindrical projectile.(A) 0° (B) 15° (C) 30° (D) 45°.

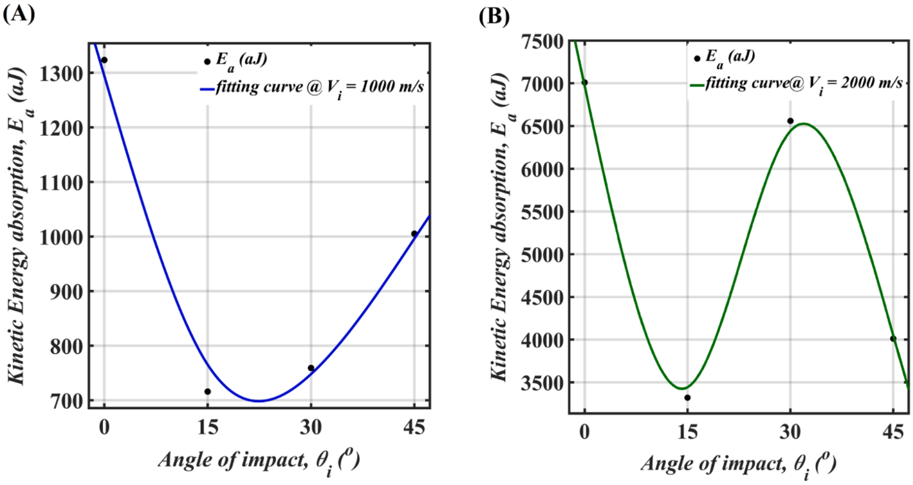

Fig. 7. Effect of obliqueness in impact angle. Comparison of the kinetic energy absorbed by *RVE*-5 when subjected to the oblique impact with different angles of impact at the projectile velocity of (A) 1000 m/s and (B) 2000 m/s.

of 1500 m/s the *RVE*-5 offers the highest kinetic energy absorption followed by *RVE*-(3–4) (the other *RVE* configurations reinforced with two layers of graphene). The trend of the percentage of kinetic energy absorption of the considered *RVE* configurations for the impact velocity of 1000 m/s and 2000 m/s is illustrated in Fig. 5(D). It can be noticed from Fig. 5(D) that at the impact velocity of 1000 m/s *RVE*-2 offers the maximum percentage of kinetic energy absorption (68.85%), whereas, at the impact velocity of 2000 m/s *RVE*-5 offers the maximum percentage of kinetic energy absorption (81.51%). In summary, the results reported in this subsection indicate that the stacking sequence of *Al* and graphene layers followed for the *RVE*-3 offers the resistance to complete penetration (i.e. maximum resistance to penetration) and *RVE*-5 offers the higher magnitude of kinetic energy absorption for the highest impact velocity (2000 m/s) used in the present study. We would further propose hybrid configurations in the preceding subsections based on *RVE*-3 and *RVE*-5 to have both complete penetration resistance and high energy absorption capacity simultaneously (refer to Fig. 12).

3.2. *Effect of oblique impact of the projectile*

This subsection examines the effect of the projectile's angle of incidence on the ballistic performance of graphene-reinforced *Al* laminate. The *RVE*-5 is chosen to investigate the oblique impact of a projectile due to its superior performance in terms of kinetic energy absorption when subjected to high-velocity impact. The *RVE*-5 configuration is subjected to the oblique impact, wherein an angle of incidence varies from 0° to 45° with an interval of 15° (refer to Fig. 6). The oblique impact is evaluated at two different impact velocities, 1000 m/s, and 2000 m/s. The kinetic energy absorbed by the structure is observed for each instance and illustrated in Fig. 7. It is noticed that the *RVE*-5 configuration absorbs the highest kinetic energy when the angle of incidence is 0°, followed by 15° at the impact velocity of 1000 m/s. When the impact velocity is increased from 1000 m/s to 2000 m/s the transverse impact of the projectile (0°) resulted in the highest kinetic energy absorption. It is also evident from Fig. 7 that at the oblique angle of 15° the kinetic energy absorbed by the *RVE*-5 decreases regardless of the impact velocity. Thus the results show the importance of considering the obliqueness of impact angle, which is inevitable in most practical situations, while evaluating the energy absorption capacity for designing graphene-reinforced composites subjected to ballistic impact.

The normal (*z*) component of displacement and velocity of projectiles is observed for the cases of oblique impact to assess the normal depth traveled by the projectile and its residual velocity in the normal direction, respectively (refer to Fig. 8). The observations presented in Fig. 8 provide a clear insight into the influence of the projectile's angle of incidence on the post-impact behavior exhibited by *RVE*-5. The post-

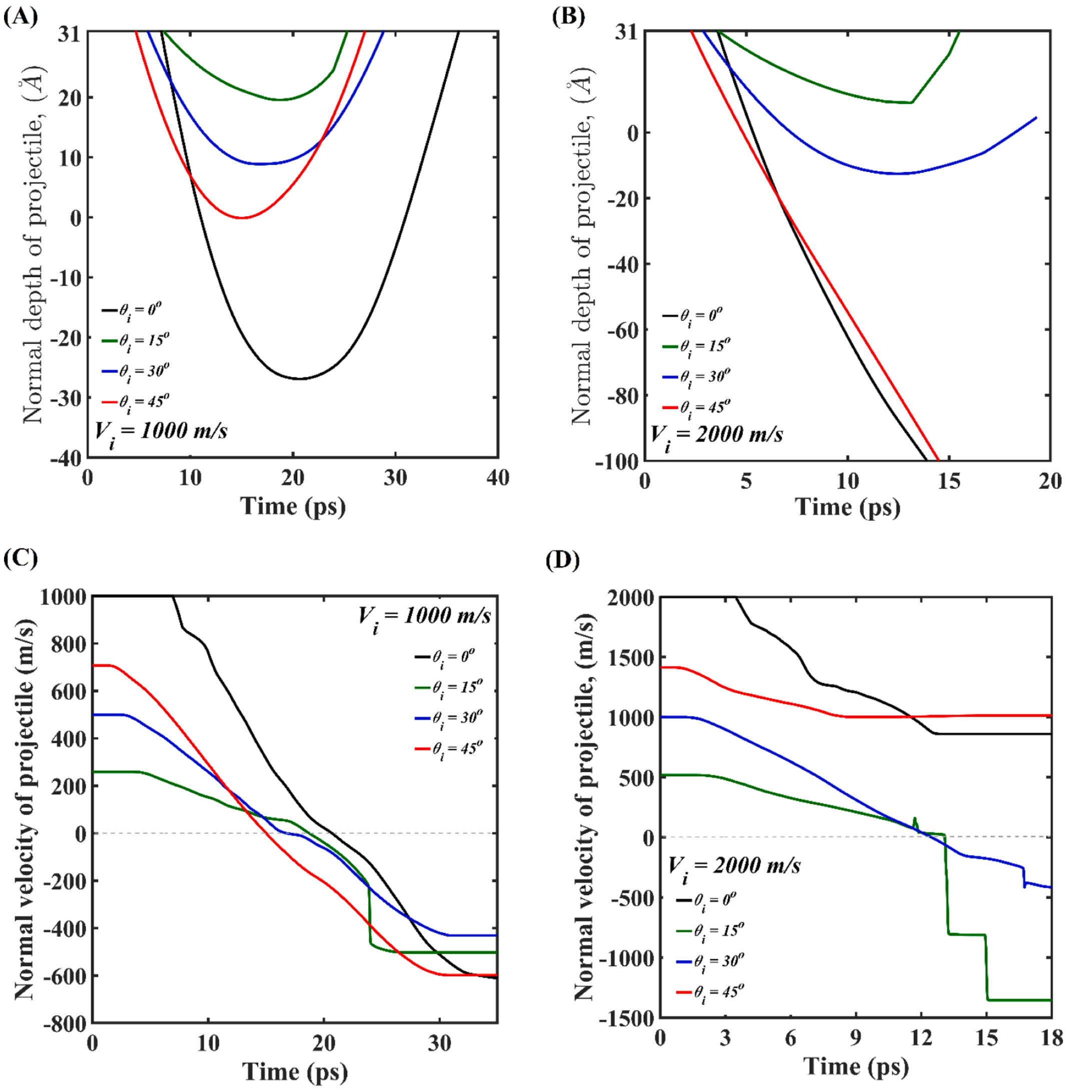

Fig. 8. Time-history of projectiles. (A) Normal depth at different angles of impact for the impact velocity of 1000 m/s (B) Normal depth at different angles of impact for the impact velocity of 2000 m/s (C) Normal velocity at different angles of impact for the impact velocity of 1000 m/s (D) Normal velocity at different angles of impact for the impact velocity of 2000 m/s.

impact travel of the projectile in the normal direction is illustrated in Fig. 8(A) and Fig. 8(B) at the initial impact velocity of 1000 m/s and 2000 m/s, respectively. The corresponding variations in the normal component of velocity are presented in Fig. 8(C) and Fig. 8(D) at the initial impact velocity of 1000 m/s and 2000 m/s, respectively. The highest target (*RVE*-5) deflection corresponding to the normal displacement of the projectile is observed for the case of transverse impact ($\theta = 0°$), followed by 45°, 30° and 15° at the impact velocity of 1000 m/s (refer to Fig. 8(A)). Note that the cases with relatively higher deflection (0° and 45° at the impact velocity of 1000 m/s) resulted in high kinetic energy absorption, which may be associated with the high elastic deformation of *RVE*-5. At the initial impact velocity of 1000 m/s, *RVE*-5 offers a rebound of the projectile regardless of the angle of incidence (refer to Fig. 8(C)). In the cases of oblique impact, the least and highest normal component of residual velocity is observed for the cases of 30° and 45°, respectively, at the impact velocity of 1000 m/s. The observations presented in the preceding sections indicate that *RVE*-5 exhibits complete penetration in the case of transverse impact of projectile at the impact velocity of 2000 m/s. A similar observation is noted in the case of the projectile's impact at 45°. In contrast, with the oblique impact at the angles of 15° and 30°, *RVE*-5 exhibits a rebound of the projectile at the impact velocity of 2000 m/s (refer to Fig. 8(B, D)). However, the rebound of projectile occurs with a substantial damage in the top layer of graphene and *Al* laminate (refer to Fig. 9 (A-B)). The top layer of *RVE*-5 causes post-impact sliding motion of the projectile followed by the penetration damage before the rebound of projectile for the cases of 15° and 30° angle of impact at 2000 m/s impact velocity.

In summary, regardless of the impact velocity (1000 m/s or 2000 m/s), *RVE*-5 offers better kinetic energy dissipation along with the least target deformation for the case of impact at an oblique angle of 15°. On the contrary, the high-velocity impact at an oblique angle of 45° is observed to be relatively more detrimental to the *RVE*-5 in terms of kinetic energy dissipation and extent of deflection/damage. Thus, the performance of a particular RVE is dependent on the angle of impact.

3.3. *Effect of the shape of the projectile*

In this subsection, the influence of the shape of the projectile on the kinetic energy absorption capability of the *RVE*-5 configuration is illustrated. The *RVE*-5 configuration is chosen to conduct this study for the same reason as stated in subsection 3.2. In this regard, the projectile is modeled using three different shapes (cylindrical, spherical, and partial conical) as depicted in Fig. 10(A-C). For a fair comparison, the mass of the differently shaped projectiles is maintained the same by

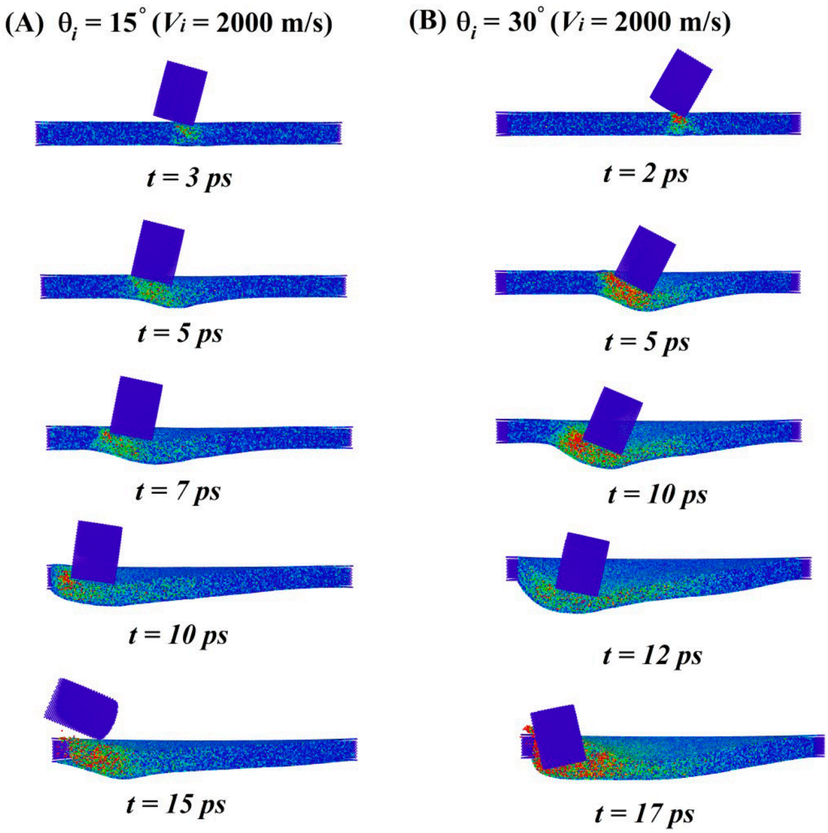

Fig. 9. Atomistic snapshots of oblique high-velocity impact. Results are shown at angle (A) 15° and (B) 30° with an impact velocity of 2000 m/s.

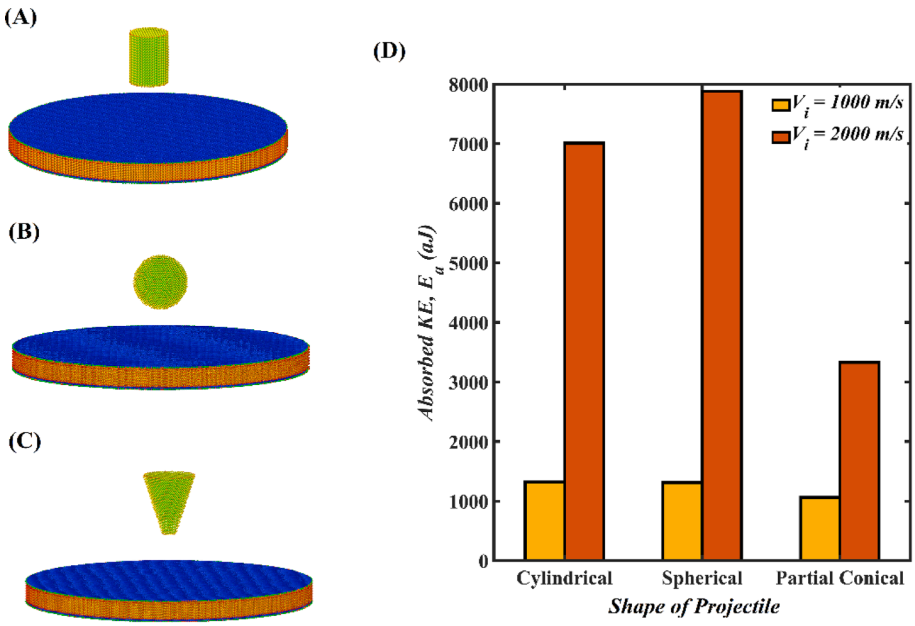

Fig. 10. Projectile's shape-dependent kinetic energy absorption of *RVE*-5. (A) Atomistic model of *RVE*-5 and cylindrical projectile (B) Atomistic model of *RVE*-5 and spherical projectile (C) Atomistic model of *RVE*-5 and partial conical projectile (D) Comparison of kinetic energy absorption of *RVE*-5 when the projectile's shape is varied at the impact velocity of 1000 m/s and 2000 m/s.

keeping the volume of the projectiles constant ($\approx 2.0e^5$ Å^3). The observations of the projectile's shape-dependent kinetic energy absorption of the *RVE*-5 configuration are illustrated in Fig. 10(D). It is evident from the results that at the impact velocity of 1000 m/s the cylindrical projectile results in higher kinetic energy absorption when compared with the other shapes of the projectile. However, when the impact velocity is increased to 2000 m/s, the spherical projectile leads to the highest kinetic energy absorption. The impact by the partial conical projectile resulted in the least kinetic energy absorption of *RVE*-5, regardless of the impact velocity. The traveling depth and velocity profile of the projectile

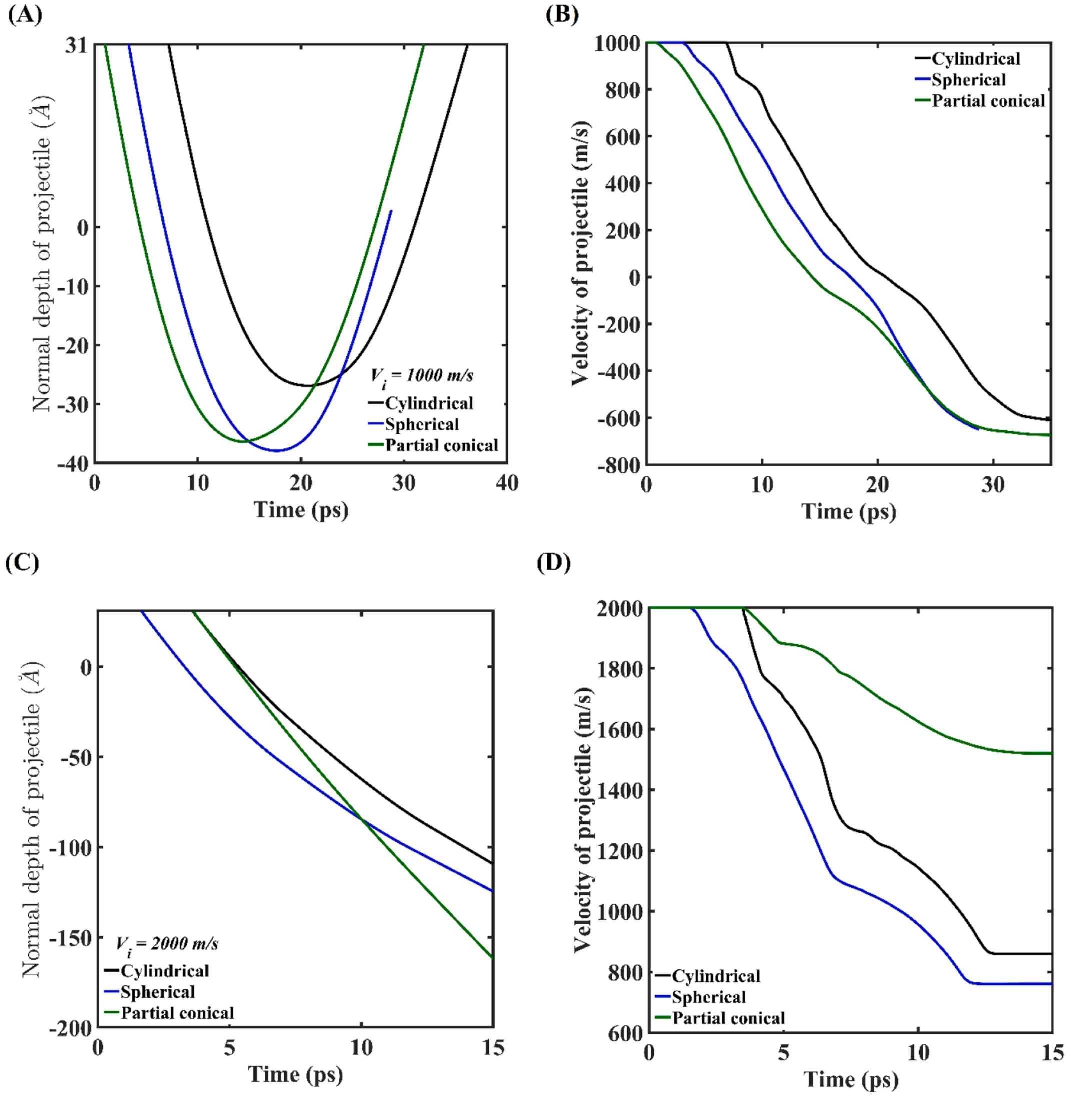

Fig. 11. Time-history of projectiles. (A) Traveling depth of projectiles at the initial impact velocity of 1000 m/s (B) Temporal variation in the velocity of projectiles at the initial impact velocity of 1000 m/s (C) Traveling depth of projectiles at the initial impact velocity of 2000 m/s (D) Temporal variation in the velocity of projectiles at the initial impact velocity of 2000 m/s.

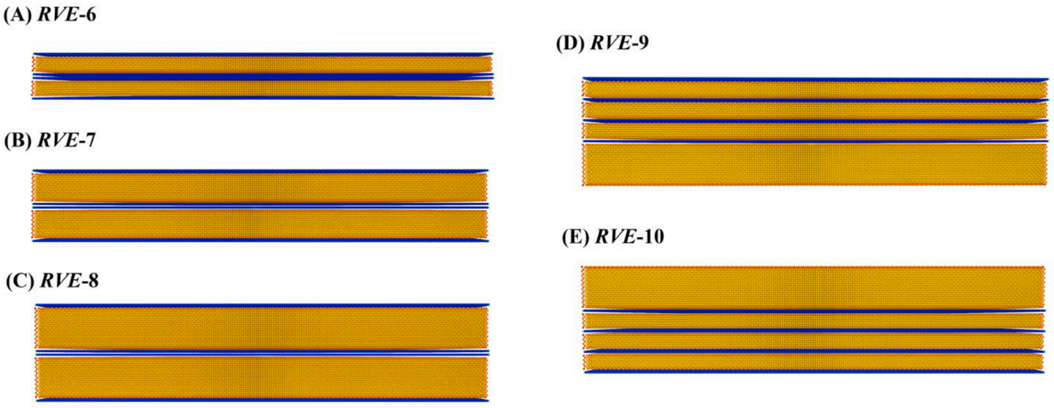

Fig. 12. Hybrid *RVE*s with strategic stacking sequences of graphene and *Al* laminates. (A) *RVE*-6: Combination of the stacking sequence followed for *RVE*-3 and *RVE*-5, with the effective thickness of *Al* as 6*a* (B) *RVE*-7: Combination of the stacking sequence followed for *RVE*-3 and *RVE*-5, with the effective thickness of *Al* as 12*a* (C) *RVE*-8: Combination of the stacking sequence followed for *RVE*-3 and *RVE*-5, with the effective thickness of *Al* as 18*a* (D) *RVE*-9: The graphene layers are concentrated at the target face of *RVE*, with the effective thickness of *Al* as 18*a* (E) *RVE*-9: The graphene layers are concentrated at the rear face of *RVE*, with the effective thickness of *Al* as 18*a*.

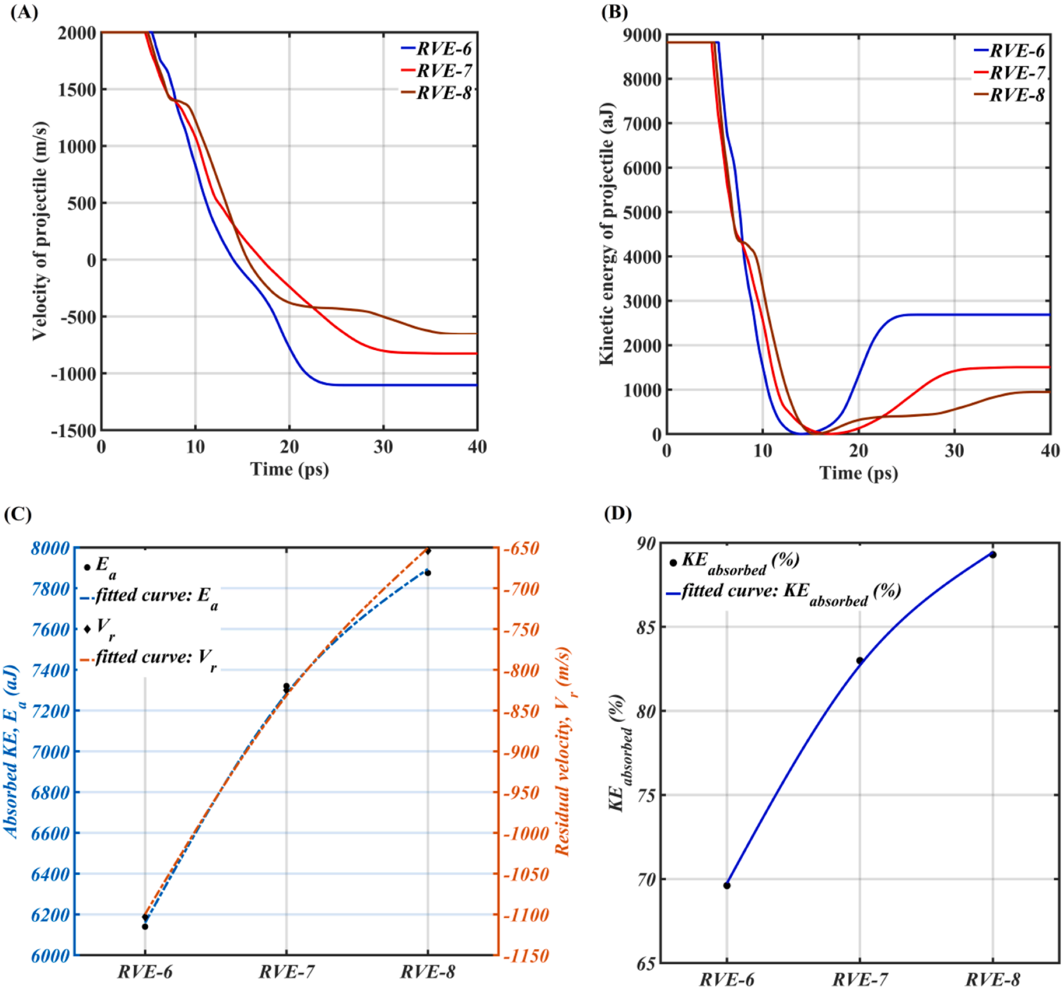

Fig. 13. Ballistic performance of strategically sequenced hybrid *RVE*s-(6–8). (A) Comparison of the time-history of the velocity of projectile for different *RVE*s-(6–8) when impact velocity is 2000 m/s (B) Comparison of the time-history of the kinetic energy of projectile for different *RVE*s-(6–8) when impact velocity is 2000 m/s (C) Variation in kinetic energy absorption and residual velocity of the projectile for *RVE*s-(6–8) (D) Variation in the percentage of kinetic energy absorption for *RVE*s-(6–8).

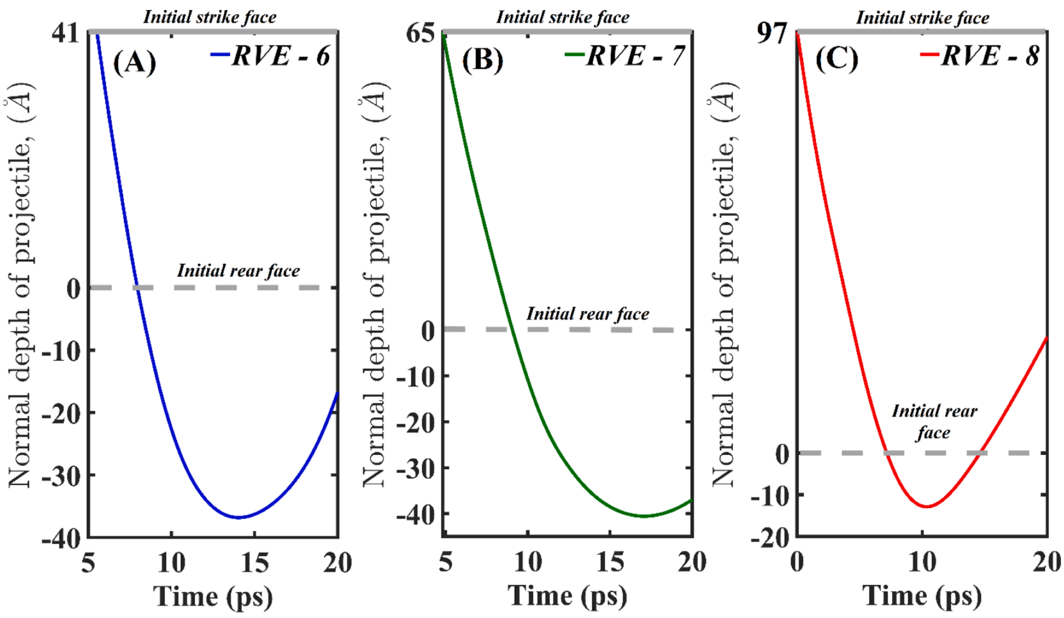

Fig. 14. Normal displacement of the projectile for the cases of (A) *RVE*-6 (B) *RVE*-7 and (C) *RVE*-8.

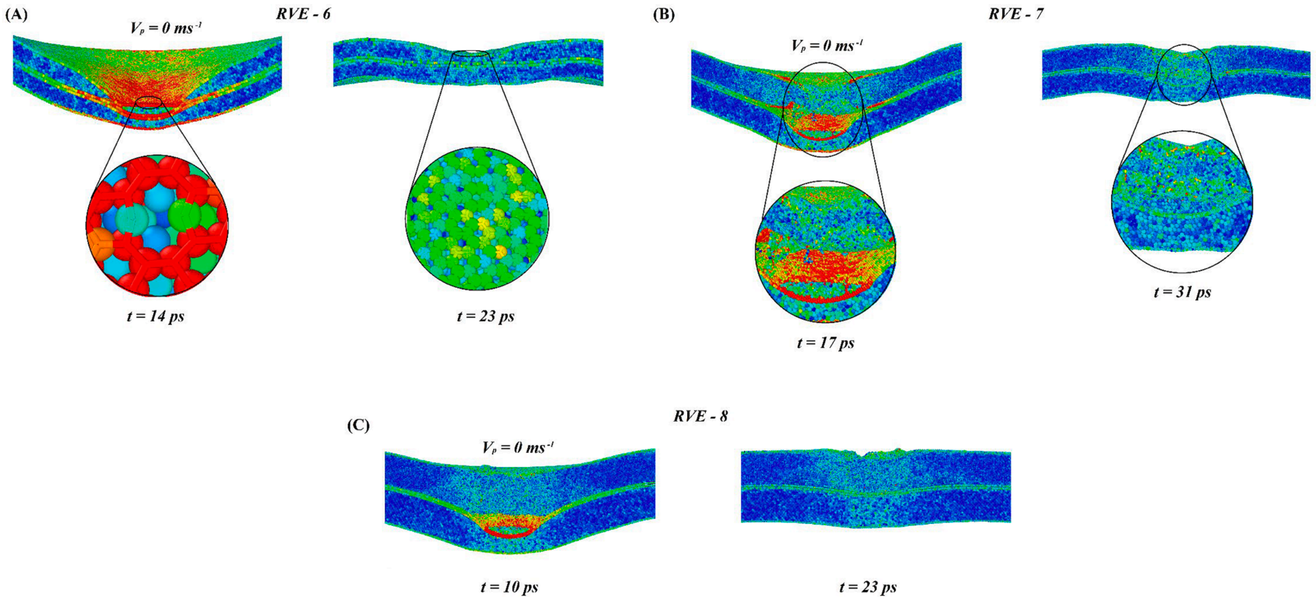

Fig. 15. Deflection/damage caused by high-velocity impact of projectiles. (A) *RVE*-6 (B) *RVE*-7 and (C) *RVE*-8. The left-hand side image for each case corresponds to the deflection/damage when the projectile velocity is zero and the right-hand side image for each case corresponds to permanent damage sustained by *RVE*s.

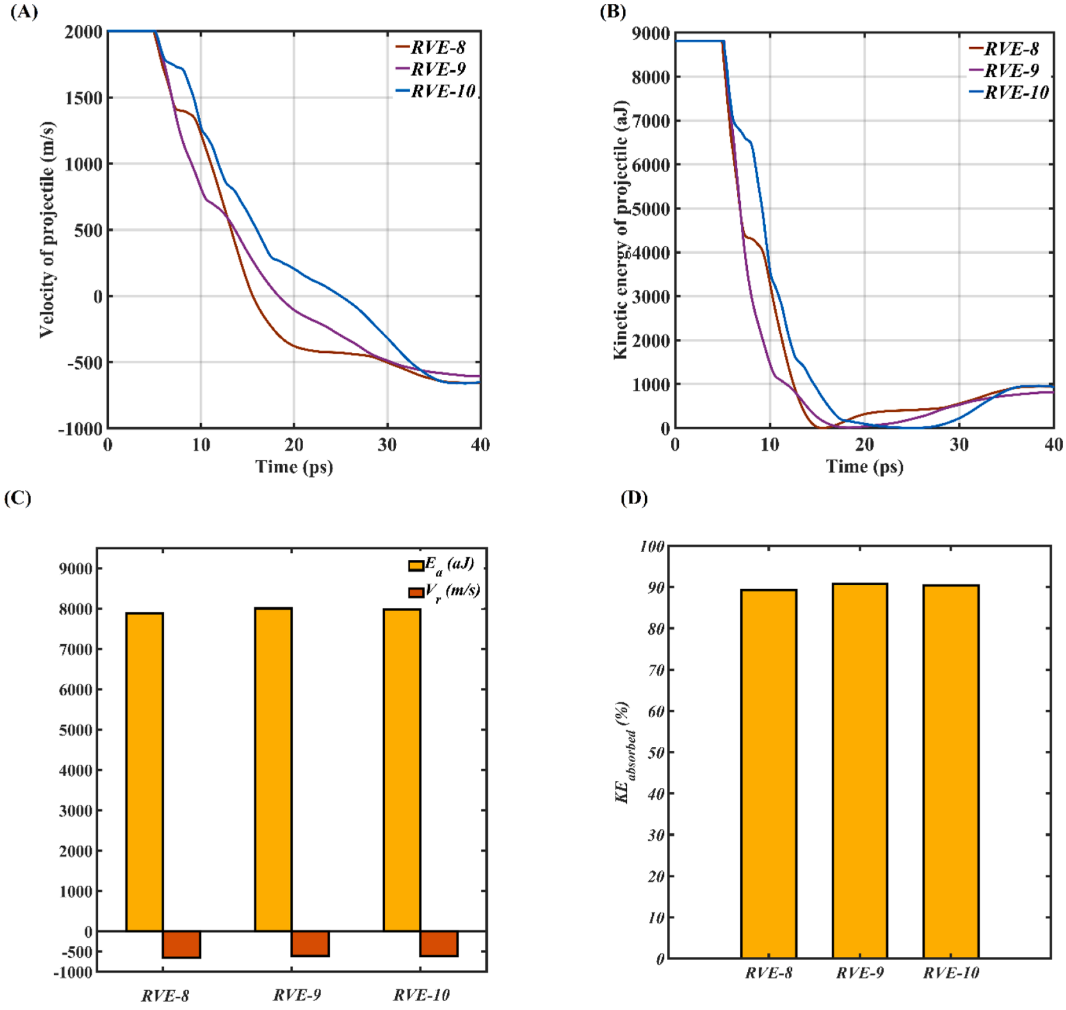

Fig. 16. Comparative ballistic performance of *RVE*s-(8–10). (A) Comparison of time-history of the velocity of projectile for different *RVE*s-(8–10) when impact velocity is 2000 m/s (B) Comparison of time-history of the kinetic energy of projectile for different *RVE*s-(8–10) when impact velocity is 2000 m/s (C) Variation in kinetic energy absorption and residual velocity of the projectile for *RVE*s-(8–10) (D) Variation in the percentage of kinetic energy absorption for *RVE*s-(8–10).

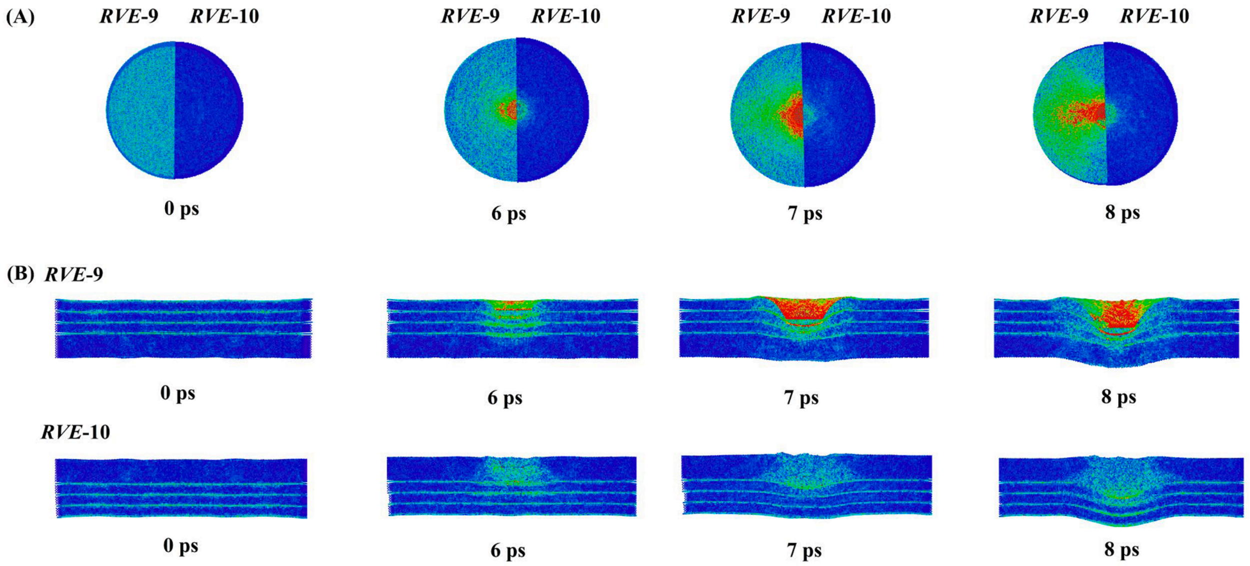

Fig. 17. Post-impact Von-Mises stresses distribution in the *RVE*-9 and *RVE*-10. (A) longitudinal (in-plane) direction (B) transverse direction. In Fig. 17(A) the first half corresponds to the *RVE*-9 and the second half corresponds to the *RVE*-10.

illustrated in Fig. 11 highlights that at the initial impact velocity of 1000 m/s, spherical projectiles cause higher deflection followed by partial conical and cylindrical (refer to Fig. 11(A)). Also, at the impact velocity of 1000 m/s, a cylindrical projectile results in the least residual velocity when compared to other projectile shapes (refer to Fig. 11(B)). The *RVE*-5 is completely penetrated by the projectiles at the impact velocity of 2000 m/s, regardless of the projectile shapes (refer to Fig. 11 (C-D)).

3.4. Influence of the thickness of Al matrix: Hybrid configurations

The observations reported in subsection 3.1 reveal that the stacking sequence of *Al* and graphene adopted in *RVE*-3 and *RVE*-5 results in the maximum resistance to the penetration (i.e complete penetration at the maximum velocity) and maximum kinetic energy absorption, respectively (under impact velocity of 2000 m/s). Hence in this subsection, we have combined the stacking sequence of the *RVE*-3 and *RVE*-5 to model new sets of *RVE*s (hybrid configurations) illustrated in Fig. 12(A-C). The effective thickness of *Al* in *RVE*-6, *RVE*-7, and *RVE*-8 is modeled as 6*a*, 12*a,* and 18*a* (where *a* stands for the lattice constant of aluminum).

The ballistic performance of *RVE*s-(6–8) is illustrated in Fig. 13. Fig. 13(A) depicts the time history of the variation in the projectile velocity, wherein all the *RVE*s (6–8) offer the penetration resistance at the projectile's velocity of 2000 m/s. It is noteworthy to mention that when compared with the *RVE*-3, the residual velocity of the projectile for the case of *RVE*-6 slightly (≈ 4%) increases, whereas for the same stacking sequence of graphene (as *RVE*-6) increasing the effective thickness of *Al* matrix from 6*a* to 12*a* (*RVE*-7) and 18*a* (*RVE*-8) reduces the residual velocity of projectile up to 22% and 38%, respectively. The increase in the effective thickness of the *Al* matrix also results in increased kinetic energy absorption of *RVE*-(7–8) when compared to the *RVE*-6 (refer to Fig. 13(B-C)). It is evident from Fig. 13(B) that the kinetic energy profile of the projectile for *RVE*-6 exhibits a similar two distinct regions as evident for the *RVE*-3 (shown in Fig. 5(B)), wherein the projectile first reaches the zero kinetic energy and then suddenly gains the kinetic energy due to the stress wave release imposed by the graphene reinforcement. The kinetic energy profile of the projectile for *RVE*s-(7–8) illustrated in Fig. 13(B) shows that increasing the effective thickness of *Al* laminate significantly dissipates the stress wave release of the graphene reinforcements. Fig. 13(B) also shows that as the effective

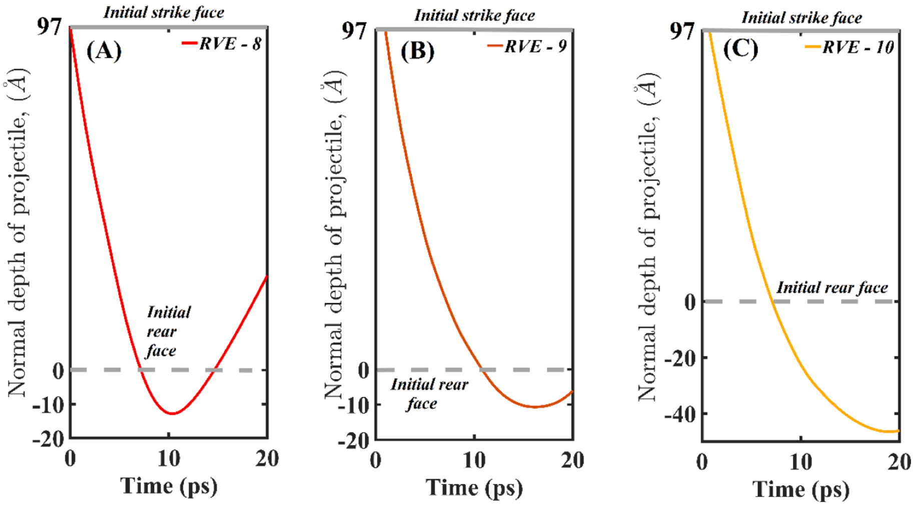

Fig. 18. Normal displacement of the projectile. (A) *RVE*-8 (B) *RVE*-9 (C) *RVE*-10.

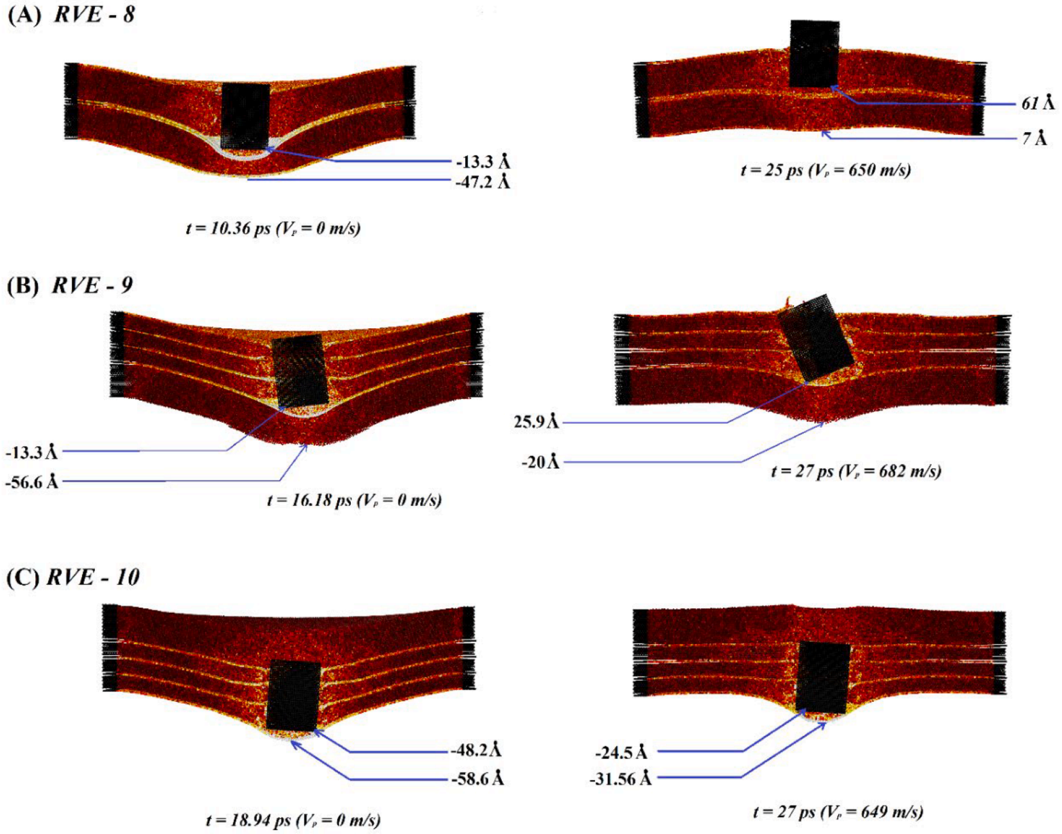

Fig. 19. Damage caused by high-velocity impact of the projectile. (A) *RVE*-8 (B) *RVE*-9 and (C) *RVE*-10. The left-hand side image for each case corresponds to the maximum state of damage when the projectile velocity reaches zero and the right-hand side image for each case corresponds to permanent damage sustained by *RVE*s.

thickness of the *Al* laminate increases, the residual kinetic energy of the projectile decreases, indicating greater capabilities of *RVE*s-(7–8) in terms of high kinetic energy dissipation. Fig. 13(C) demonstrates a similar trend. Fig. 13(D) depicts the percentage of kinetic energy absorbed by *RVE*s-(6–8), with *RVE*-8 having the highest kinetic energy absorption (≈89%), followed by the *RVE*-7 (≈83%). The extent of deformation or damage in the *RVEs* (6–8) at the impact velocity of 2000 m/s is assessed by tracking the normal displacement of the projectile, which is illustrated in Fig. 14. It is evident that as the thickness of *RVE*s increases the normal depth of projectile travel diminishes. The maximum normal depth of the projectile can be observed at the instant of zero projectile velocity. The deflection or damage of *RVE*s (6–8) is demonstrated in terms of atomistic snapshots in Fig. 15. It is evident from Figs. 14 and 15 that in the case of *RVE*-6 the target is deflected without considerable damage (refer to Fig. 15(A)), whereas in the case of *RVE*-7 and *RVE*-8 the projectile travels into the target and causes significant damage. The extent of damage is considerably lower in the case of *RVE*-8 when it is compared with *RVE*-7 (refer to Fig. 15 (B) and (C)).

With the understanding presented above, in the further analysis, we have altered the stacking sequence of graphene layers within the *Al* laminate of thickness 18*a* and modeled *RVE*-9 and *RVE*-10 as shown in Fig. 12(D-E). While modeling the *RVE*-9, the group of graphene layers is placed at the front face of the target, whereas the *RVE*-10 is modeled with the group of graphene layers at the rear face of the target. Such non-symmetric sequencing of graphene layers is utilized to find the suitable configuration of graphene reinforced aluminum composite which can exhibit the highest kinetic energy absorption without complete penetration. The ballistic performance of the *RVE*s-(9–10) is compared with *RVE*-8, which is depicted in Fig. 16. The time history of the variation in the velocity and kinetic energy of the projectile reveals that the configuration of *RVE*-9 offers the least post-impact residual velocity and kinetic energy of the projectile. Owing to that, the highest kinetic energy absorption can be noticed for *RVE*-9. However, the concerned values of *RVE*s-(8–10) are in the vicinity of each other (refer to Fig. 16(A-B)). Furthermore, the kinetic energy absorption in the *RVEs*-(8–10) is also observed to be close (refer to Fig. 16(C-D)). The penetration mechanism of the *RVE*-8 is observed similar to the *RVE*-3, where the bilayer graphene can withstand the high-velocity impact and prohibits the projectile to penetrate further (as visualized in supplementary multimedia file MM2). On contrary, the projectile penetrates to a greater depth in the case of *RVE*s-(9–10) but the distributed graphene layers at the target face (for *RVE*-9) are observed to slow down the projectile's penetration speed faster than the distributed graphene layers at the rear face (*RVE*-10) of the *RVE*s. This can be seen by comparing the velocity profiles of the projectiles in the cases of *RVE*-9 and *RVE*-10, as shown in Fig. 16(A) (as visualized in the supplementary multimedia file MM3 and MM4).

The post-impact stress distribution in *RVE*-9 and *RVE*-10 is compared in Fig. 17, wherein the stress distribution along the in-plane (i.e. longitudinal) and transverse direction of the structures is revealed. Fig. 17 (A) depicts the comparison of the stress distribution in the longitudinal directions of the structures, where the first half of the structure shows

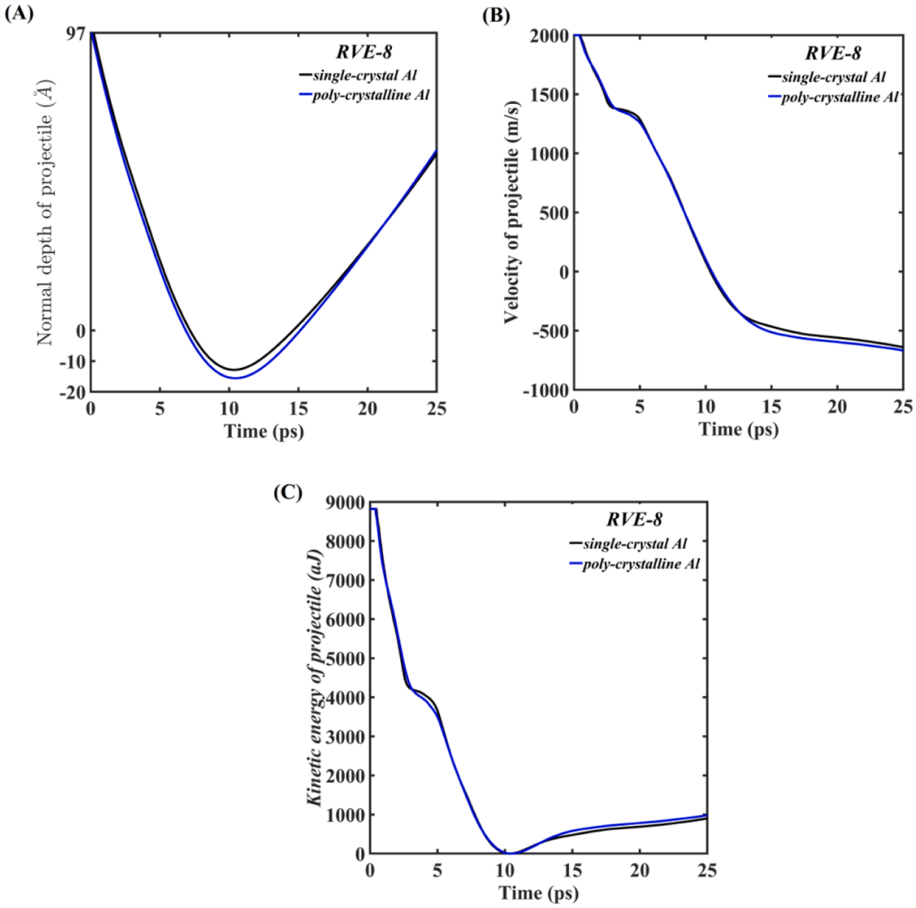

Fig. 20. Comparative perspective of impact responses for *RVE*-8 modeled with single crystal *Al* and poly-crystalline *Al*. (A) Penetration depth of the projectile (B) Velocity profile of the projectile (C) Kinetic energy profile of projectile.

the distribution of stress in the target face of *RVE*-9, and the second half shows the distribution of stress in the target face of *RVE*-10. Fig. 17(B) shows the stress distribution in the transverse direction of *RVE*-9 and *RVE*-10. It is revealed from Fig. 17 that the stress generated in the structure due to high-velocity impact is majorly distributed by the graphene reinforcements, especially in the case of *RVE*-9. Fig. 17 shows that the *RVE* configuration with the graphene at the point of impact (*RVE*-9) majorly distributes the stress, whereas the *RVE* configuration with the *Al* laminate at the point of impact (*RVE*-10) majorly shows the localized distribution of the stress in the transverse direction instead of the longitudinal direction.

The penetration damage in the *RVE*s-(8–10) is illustrated in Fig. 18 and Fig. 19. Fig. 18 depicts the extent of normal penetration depth of the projectile in the *RVE*s-(8–10), wherein it is revealed that for the cases of *RVE*-8 and *RVE*-9 the traveled depth of the projectile is the same (refer to Fig. 18(A-B)), whereas *RVE*-10 exhibits higher penetration depth of the projectile (refer to Fig. 18(C)). Similar observations can be noticed in Fig. 19. Fig. 19 also shows that in the case of *RVE*-8, the projectile reaches zero velocity in less time than in the case of *RVE*-9 or *RVE*-10.

In summary, the investigation presented in this section proposes the operational equivalency of *RVE*s (8–10) in terms of kinetic energy dissipation and residual velocity of the projectile. However, the extent of damage is observed to be higher in the case of *RVE*-10 when compared with *RVE*-8 and *RVE*-9. Further to understand the influence of poly-crystalline *Al* laminates on the ballistic performance of graphene-reinforced *Al* thin film structures, *RVE*-8 and *RVE*-9 are separately modeled by using poly-crystalline (9 crystals) *Al* laminates, and the simulation of high-velocity impact is performed at the impact velocity of 2000 m/s. The comparison of variations in penetration depth, velocity, and kinetic energy of the projectile for single-crystal *Al* and poly-crystalline *Al* based *RVE*-8 is presented in Fig. 20, which shows negligible variations in the profile of projectile. The comparison of variations in penetration depth, velocity, and kinetic energy of the projectile for single-crystal *Al* and poly-crystalline *Al* based *RVE*-9 is presented in Fig. 21. Unlike, *RVE*-8, the poly-crystalline *Al* has slightly more influence on the ballistic performance of *RVE*-9, wherein, the poly-crystalline *Al* based *RVE*-9 shows less residual velocity and kinetic energy with lower projectile penetration. This can be explained by the shear strain distribution along the grain boundaries of poly-crystalline *Al,* which restricts the excessive deformation of *RVE*-9 as shown in Fig. 22 (B). The single-crystal *Al* based *RVE*s (*RVE*-(8–9)) exhibit localized distribution of shear strain within the impact zone (refer to Fig. 22(A and C)), whereas in the cases of poly-crystalline *Al* based RVEs the shear strain is distributed along the grain boundaries (refer to Fig. 22 (B and D)). In general, Figs. 20 and 21 show that the trends of impact behavior do not change significantly for single and poly-crystalline *Al* based RVEs.

With the insights gathered from the analysis presented in the preceding subsections, it is realized that the stacking sequence followed in *RVE*-9 results in the highest kinetic energy absorption with the least rebound velocity in the projectile for the highest impact velocity (i.e. no

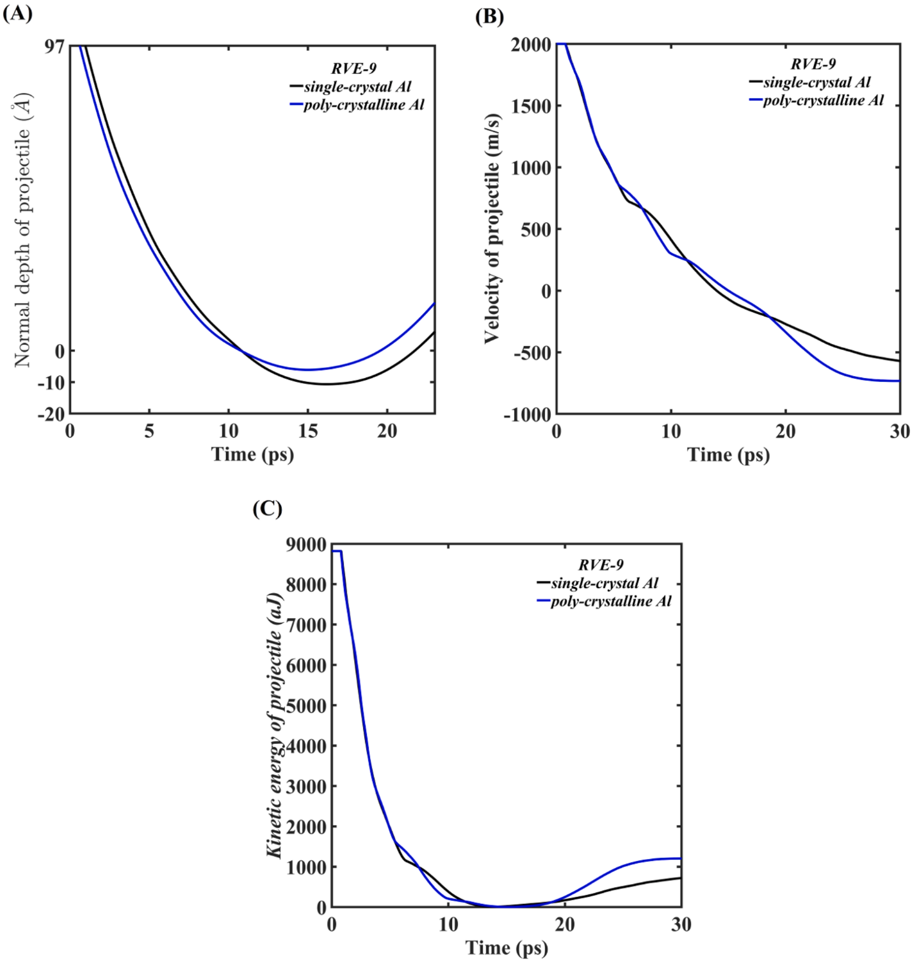

Fig. 21. Comparative perspective of impact responses for *RVE*-9 modeled with single crystal *Al* and poly-crystalline *Al*. (A) Penetration depth of the projectile (B) Velocity profile of the projectile (C) Kinetic energy profile of projectile.

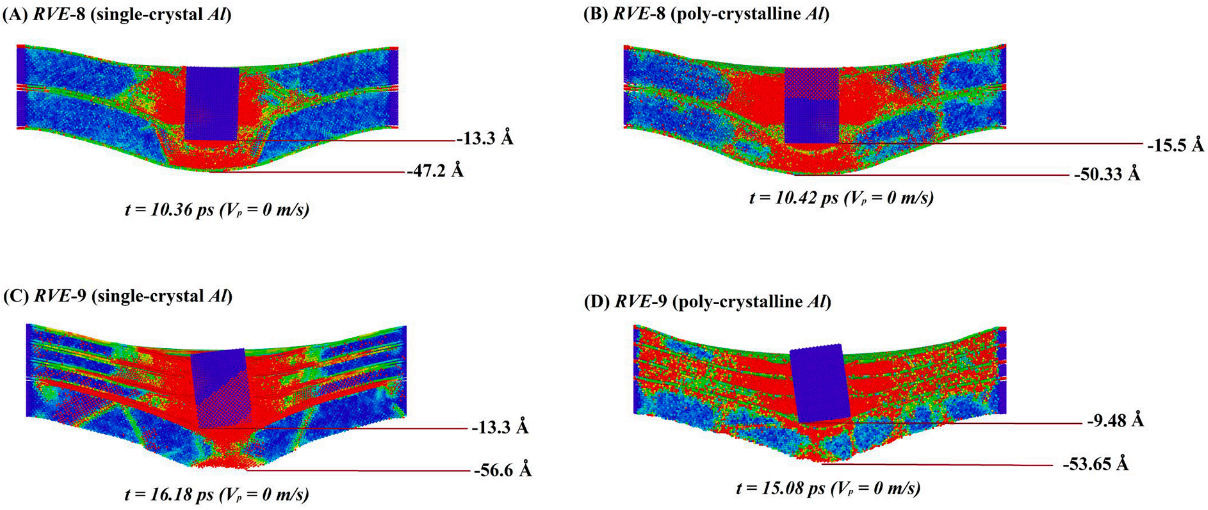

Fig. 22. Comparative perspective of post-impact shear strain distributions modeled with single crystal *Al* and poly-crystalline *Al*. (A) *RVE*-8 modeled with single-crystal *Al* (when the projectile velocity is zero) (B) *RVE*-8 modeled with poly-crystalline *Al* (when the projectile velocity is zero). (C) *RVE*-9 modeled with single-crystal *Al* (when the projectile velocity is zero) (D) *RVE*-9 modeled with poly-crystalline *Al* (when the projectile velocity is zero).

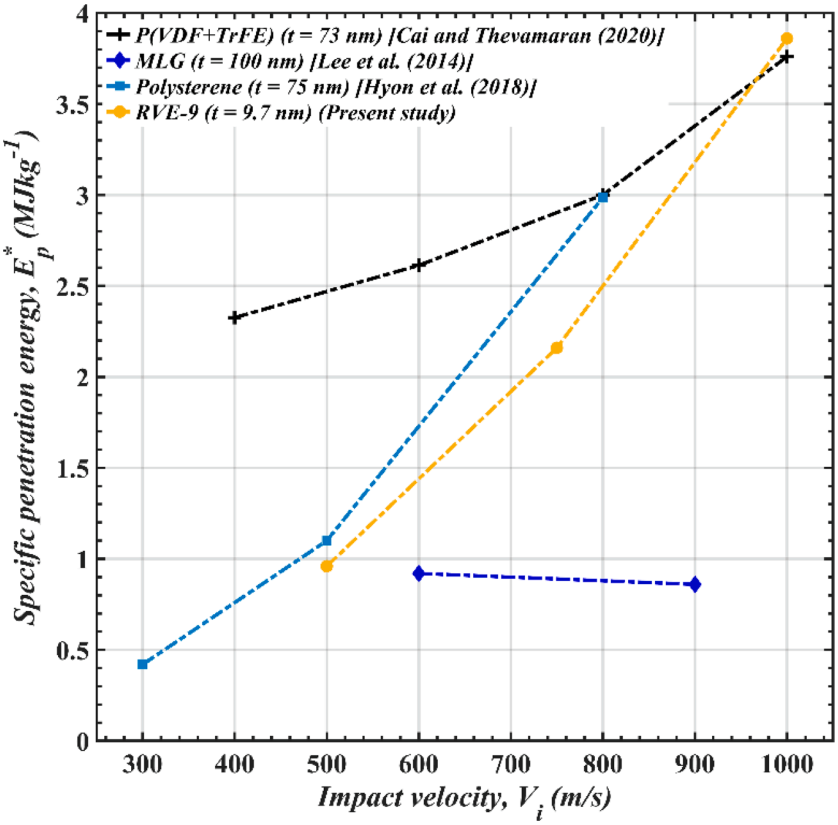

Fig. 23. Benchmarking the performance of *RVE*-9. Comparison of the specific penetration energy (E_p*) of *RVE*-9 with other barrier materials (Cai and Thevamaran [62], Lee *et al.* [10], Hyon *et al.* [63]). Here '*t*' in the legends indicate the corresponding thickness of the thin film structures.

penetration). Hence, we have compared the MD simulations based on specific penetration energy (E_p*) of *RVE*-9 with the recently observed superior barrier materials based on the microprojectile impact test [10,62,63] (refer to Fig. 23). It is worth noting that observations reported by Lee *et al.* [10], Cai and Thevamaran [62], and Hyon *et al.* [63] are based on the high-velocity impact of micro-projectiles, where the impact performance is assessed on the basis of specific penetration energy (E_p*). The value of E_p* reflects the localized impact performance of the material by normalizing the penetration energy with the mass of the impact zone. The penetration cases illustrated in our investigation demonstrate that the graphene/*Al* laminates exhibit localized penetration; hence it is rational to use the E_p* value of *RVE*-9 for the comparison of their performance with previously reported superior barrier materials. With this understanding, the observations depicted in Fig. 23 reveal that even with a substantially lower thickness of *RVE*-9 when compared with other structures, it exhibits comparable specific penetration energy. This indicates that such alternatively stacked *Al* and graphene layers can be potentially useful barrier materials against high-velocity impact. In summary, the hybrid configurations *RVEs*-(6–8) can achieve both high energy absorption capability and resistance to complete penetration simultaneously, proving to be better than *RVEs*-(1–5). Note that *RVE*-5 and *RVE*-3 show high energy absorption and no complete penetration capabilities individually, corroborating these two configurations to be better than *RVE*-1, *RVE*-2 and *RVE*-4. Further improvement in the ballistic performance can be realized in *RVE*-9, when the graphene layers are provided in the impacting half of the thickness.

3.5. *Influence of random manufacturing defects in graphene*

It is realized by several research groups in the past that the synthesis of graphene on a mass scale can produce different inherent structural irregularities in the freestanding mono-layers and bilayers of graphene. This has motivated us to explore the practically-relevant influence of random defects (missing carbon atoms) in graphene reinforcements on the ballistic performance of *Al* matrix composite. In this regard, the stacking sequence of *RVE*-9 is followed by using defective graphene layers with varying defect concentrations. By randomly removing carbon atoms (within the region of effective radius 200 Å) of graphene monolayers), different percentages (0.1 %, 0.5 %, 1 %, 1.5 %, 2 %, 2.5 % and 3 %) of defect concentrations are induced in the graphene reinforcements. The defective graphene layers are then stacked with the *Al* laminates by following the *RVE*-9 stacking sequence. Such *RVE*-9 structures reinforced with defective graphene layers are impacted by the cylindrical projectile at an impact velocity of 2000 m/s to observe the variation in the kinetic energy absorption (E_a) of the structure and residual velocity (V_r) of the projectile (refer to Fig. 24). It is observed that even a small magnitude (0.1%) of single vacancy defects in the graphene reinforcements can decrease the kinetic energy absorption by nearly 10% (refer to Fig. 24(B)), however, the occurrence of the complete penetration is realized for the cases beyond 1% defects concentration (refer to Fig. 24(C)). It is also observed that as the defects percentage increases from 0% to 1%, the penetration depth of the projectile increases by 85% (refer to Fig. 25). Such outcomes ascertain the necessity of accounting for different forms of random disorder in analyses and of graphene-reinforced *Al* laminates for an inclusive and reliable design

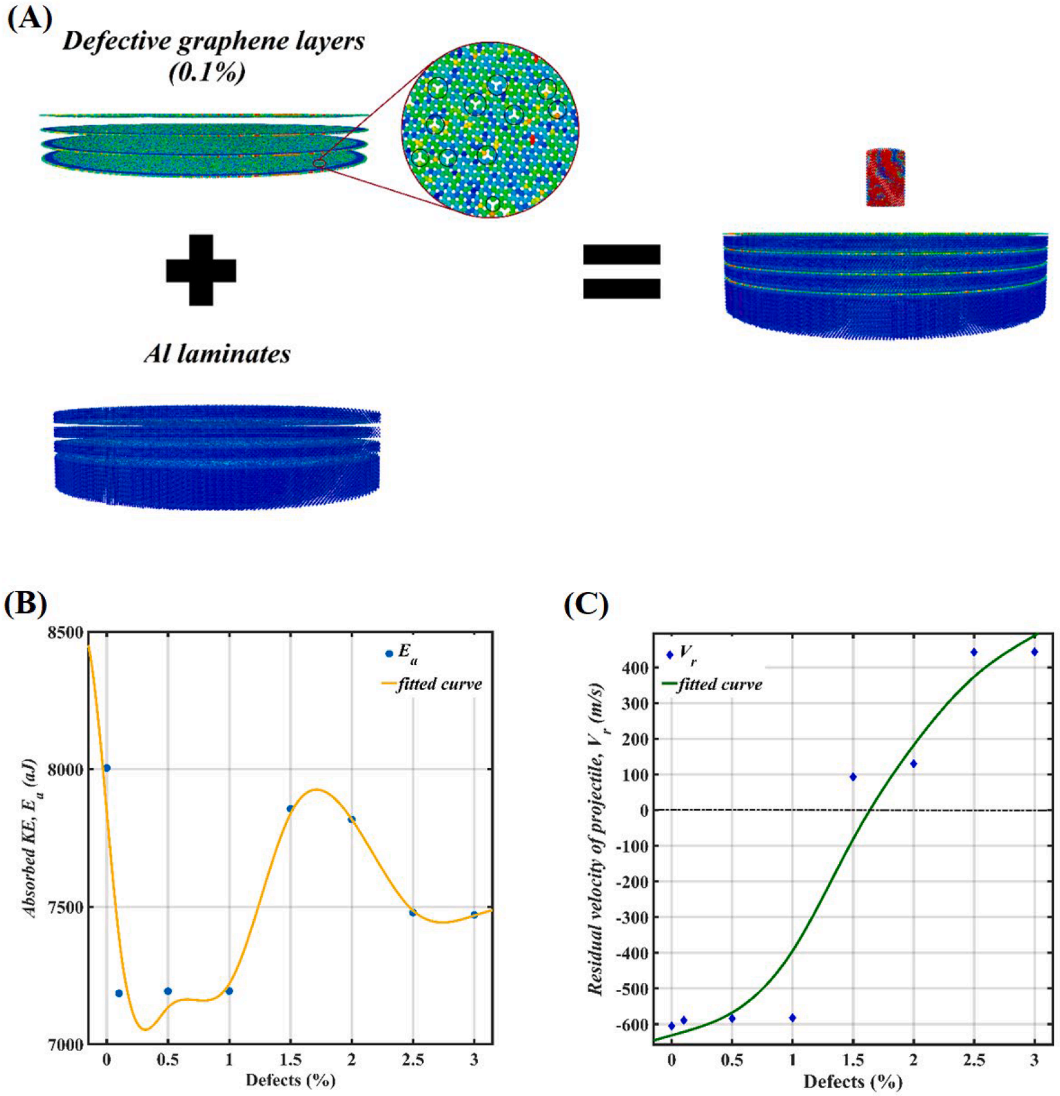

Fig. 24. Influence of defect in graphene for *RVE*-9 on the ballistic performance. (A) Stacking defective graphene monolayers in the *RVE*-9 configuration (B) Variation in the kinetic energy absorption (E_a) as a function of defect concentration in graphene **(C)**Variation in the residual velocity (V_r) of projectile as a function of defect concentration in graphene.

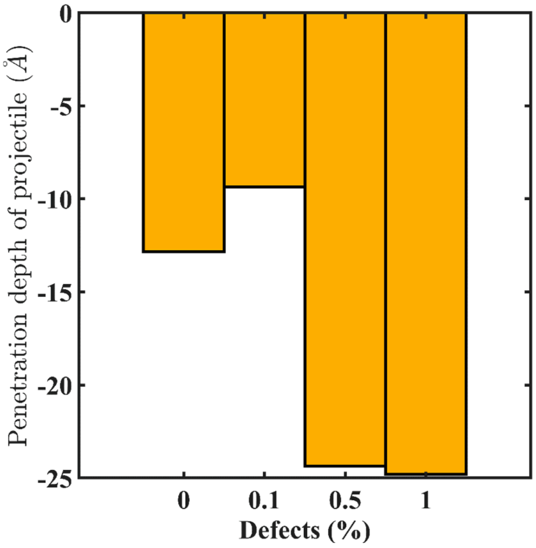

Fig. 25. Variation in the penetration depth of the projectile with the increase in defects percentage of graphene in *RVE*-9.

paradigm.

4. Conclusions

In the present study, we have performed a series of molecular-level simulations concerning high-velocity impact on graphene-reinforced *Al* laminates with the objective of identifying the most effective laminate sequence for multi-objective performances based on understanding the underlying ballistic mechanics. It is observed that strategic sequencing of the graphene layers within the aluminum matrix can significantly enhance the kinetic energy absorption of composites, while preventing penetration. In this regard, the representative volume elements (*RVEs*) consisting of the varied stacking sequences of *Al* layers and graphene are subjected to the high-velocity impact of cylindrical projectiles. The superior ballistic performance of different configurations of graphene/*Al* laminates is ascertained by quantifying the kinetic energy absorbed by each structure and the residual velocity of the projectile. At the first stage of the analysis, we have established that the reinforcement of graphene within the thin *Al* (thickness = 6*a*) film can significantly increase its capacity to withstand high-velocity impact without penetration, but it also induces a high residual velocity in the projectile. In the case of graphene-reinforced *Al* laminates, the stress generated in the material system due to high-velocity impact is dissipated significantly by the graphene reinforcements, resulting in a high post-impact stress wave release due to the elastic nature of graphene. This problem is resolved by increasing the effective thickness of *Al* layers while keeping the number of graphene layers the same. By increasing the effective thickness of *Al* (from 6a to 18a) the kinetic energy absorption of the structure is enhanced by 20% with a 40% decrease in the residual velocity of the projectile. Based on the insights gained by the first part of the study, we have proposed hybrid multifunctional configurations by combining two individual configurations with high energy absorption and no-penetration, respectively. Subsequently, we have demonstrated that a higher concentration of graphene reinforcement near the composite's target face results in approximately 90.77% kinetic energy absorption. As an integral part of the study, we have explored the influence of oblique impact angles and inevitable random disorder in the 2D nanostructure, providing a practically-relevant perspective of the outcomes. The findings of the present study will be critical in revealing the necessary in sights into the kinetic energy absorption mechanism at the nanoscale for developing high-performance multi-functional composite barrier materials. Such composites can be used in a variety of applications, including the development of lightweight body armors and surface coatings for military personnel, bulletproof automotive structures, aerospace and flight structures, and materials for turbine blades to resist shock loading caused by supersonic particle impact.

Funding and acknowledgments

KKG is grateful for financial support from the Ministry of Education (MoE), India, during this work. TM acknowledges the initiation grant received from IIT Kanpur during this work. We acknowledge National Supercomputing Mission (NSM) for providing computing resources of 'PARAM Shakti' at IIT Kharagpur, which is implemented by C-DAC and supported by the Ministry of Electronics and Information Technology (MeitY) and Department of Science and Technology (DST), Government of India.

CRediT authorship contribution statement

K.K. Gupta: Conceptualization, Investigation, Methodology, Software, Validation, Formal analysis, Visualization, Writing – original draft. **T. Mukhopadhyay:** Conceptualization, Methodology, Supervision, Writing – review & editing. **S. Dey:** Conceptualization, Methodology, Supervision, Writing – review & editing.

Declaration of Competing Interest

The authors declare that they have no known competing financial interests or personal relationships that could have appeared to influence the work reported in this paper.

Data availability

The data that support the findings of this study are available from the corresponding author, [TM], upon reasonable request.

Appendix A. Supplementary material

Supplementary data to this article can be found online at https://doi.org/10.1016/j.apsusc.2023.156502.

References

[1] A.F. Ávila, A.S. Neto, H.N. Junior, Hybrid nanocomposites for mid-range ballistic protection, Int. J. Impact Eng 38 (8–9) (2011) 669–676.

[2] M.R. O'Masta, B.P. Russell, V.S. Deshpande, An exploration of the ballistic resistance of multilayer graphene polymer composites, Extreme Mech. Lett. 11 (2017) 49–58.

[3] M.S. Nitin, S. Suresh Kumar, Ballistic performance of synergistically toughened Kevlar/epoxy composite targets reinforced with multiwalled carbon nanotubes/graphene nanofillers, Polym. Compos. 43 (2) (2022) 782–797.

[4] K. Steinke, L. Groo, H.A. Sodano, Laser induced graphene for in-situ ballistic impact damage and delamination detection in aramid fiber reinforced composites, Compos. Sci. Technol. 202 (2021), 108551.

[5] U.O. Costa, L.F.C. Nascimento, J.M. Garcia, S.N. Monteiro, F.S.D. Luz, W. A. Pinheiro, F.D.C. Garcia Filho, Effect of graphene oxide coating on natural fiber composite for multilayered ballistic armor, Polymers 11 (8) (2019) 1356.

[6] I.G. Crouch, Body armour–New materials, new systems, Defence Technology 15 (3) (2019) 241–253.

[7] Chircan, E., Gheorghe, V. and Tarnoveanu, C.R., 2020. The use of composite materials in the automotive industry.

[8] E. Grossman, I. Gouzman, R. Verker, Debris/micrometeoroid impacts and synergistic effects on spacecraft materials. MRS Bull., 35(1), pp.41-47, 2010.

[9] T.J. Carter, Common failures in gas turbine blades, Eng. Fail. Anal. 12 (2) (2005) 237–247.

[10] J.H. Lee, P.E. Loya, J. Lou, E.L. Thomas, Dynamic mechanical behavior of multilayer graphene via supersonic projectile penetration, Science 346 (6213) (2014) 1092–1096.

[11] A. Roy, K.K. Gupta, S. Dey, Probabilistic investigation of temperature-dependent vibrational behavior of hetero-nanotubes, Appl. Nanosci. 12 (7) (2022) 2077–2089.

[12] K.K. Gupta, T. Mukhopadhyay, A. Roy, S. Dey, Probing the compound effect of spatially varying intrinsic defects and doping on mechanical properties of hybrid graphene monolayers, J. Mater. Sci. Technol. 50 (2020) 44–58.

[13] S.I. Kundalwal, S.A. Meguid, G.J. Weng, Strain gradient polarization in graphene, Carbon 117 (2017) 462–472.

[14] C. Lee, X. Wei, J.W. Kysar, J. Hone, Measurement of the elastic properties and intrinsic strength of monolayer graphene, Science 321 (5887) (2008) 385–388.

[15] K.K. Gupta, T. Mukhopadhyay, A. Roy, L. Roy, S. Dey, Sparse machine learning assisted deep computational insights on the mechanical properties of graphene with intrinsic defects and doping, J. Phys. Chem. Solid 155 (2021), 110111.

[16] K.K. Gupta, T. Mukhopadhyay, L. Roy, S. Dey, Hybrid machine-learning-assisted quantification of the compound internal and external uncertainties of graphene: towards inclusive analysis and design, Materials Advances, 2022.

[17] K.K. Gupta, S. Dey, Effect of Temperature on the Fracture Strength of Perfect and Defective MonoLayered Graphene, in: Advances in Computational Methods in Manufacturing (pp. 793-804). Springer, Singapore, 2019.

[18] K.K. Gupta A. Roy S. Dey, Comparative study of various defects in monolayer graphene using molecular dynamics simulation, in: Advances in Applied Mechanical Engineering (pp. 539-546). Springer, Singapore, 2020.

[19] K. Saumya, K.K. Gupta, A. Roy, S. Dey, June. Effect of spatial distribution of nanopores on mechanical properties of mono layer graphene, in: IOP Conference Series: Materials Science and Engineering (Vol. 872, No. 1, p. 012187). IOP Publishing, 2020.

[20] F. Saba, S.A. Sajjadi, S. Heydari, M. Haddad-Sabzevar, J. Salehi, H. Babayi, A novel approach to the uniformly distributed carbon nanotubes with intact structure in aluminum matrix composite, Adv. Compos. Hybrid Mater. 2 (3) (2019) 540–548.

[21] L. Yang, B. Pu, X. Zhang, J. Sha, C. He, N. Zhao, Manipulating mechanical properties of graphene/Al composites by an in-situ synthesized hybrid reinforcement strategy, J. Mater. Sci. Technol. 123 (2022) 13–25.

[22] Q. Yan, B. Chen, L. Cao, K.Y. Liu, S. Li, L. Jia, K. Kondoh, J.S. Li, Improved mechanical properties in titanium matrix composites reinforced with quasi-continuously networked graphene nanosheets and in-situ formed carbides, J. Mater. Sci. Technol. 96 (2022) 85–93.

[23] Z. Tian, H. Yan, Q. Peng, L.J. Guo, S. Zhou, C. Ding, P. Li, Q. Luo, Atomistic Insights into Aluminum Doping Effect on Surface Roughness of Deposited Ultra-Thin Silver Films, Nanomaterials 11 (1) (2021) 158.

[24] S. Kumar, S.K. Pattanayek, S.K. Das, Reactivity-controlled aggregation of graphene nanoflakes in aluminum matrix: atomistic molecular dynamics simulation, J. Phys. Chem. C 123 (29) (2019) 18017–18027.

[25] J. Zhu, X. Liu, Z. Wang, Q. Yang, Wrinkles-assisted nanocrystalline formation and mechanical properties of wrinkled graphene/aluminum matrix composites, Model. Simul. Mater. Sci. Eng. 29 (5) (2021), 055017.

[26] S. Dixit, A. Mahata, D.R. Mahapatra, S.V. Kailas, K. Chattopadhyay, Multi-layer graphene reinforced aluminum–manufacturing of high strength composite by friction stir alloying, Compos. B Eng. 136 (2018) 63–71.

[27] L. Zhang, G. Hou, W. Zhai, Q. Ai, J. Feng, L. Zhang, P. Si, L. Ci, Aluminum/graphene composites with enhanced heat-dissipation properties by in-situ reduction of graphene oxide on aluminum particles, J. Alloy. Compd. 748 (2018) 854–860.

[28] Y. Xie, X. Meng, Y. Chang, D. Mao, Y. Yang, Y. Xu, L. Wan, Y. Huang, Ameliorating strength-ductility efficiency of graphene nanoplatelet-reinforced aluminum composites via deformation-driven metallurgy, Compos. Sci. Technol. 219 (2022), 109225.

[29] Z.W. Zhang, Z.Y. Liu, B.L. Xiao, D.R. Ni, Z.Y. Ma, High efficiency dispersal and strengthening of graphene reinforced aluminum alloy composites fabricated by powder metallurgy combined with friction stir processing, Carbon 135 (2018) 215–223.

[30] A. Mahata, T. Mukhopadhyay, M.A. Zaeem, Liquid ordering induced heterogeneities in homogeneous nucleation during solidification of pure metals, J. Mater. Sci. Technol. 106 (2022) 77–89.

[31] A. Mahata, T. Mukhopadhyay, M.A. Zaeem, Modified embedded-atom method interatomic potentials for Al-Cu, Al-Fe and Al-Ni binary alloys: From room temperature to melting point, Comput. Mater. Sci 201 (2022), 110902.

[32] T. Mukhopadhyay, A. Mahata, S. Adhikari, M.A. Zaeem, Probing the shear modulus of two-dimensional multiplanar nanostructures and heterostructures, Nanoscale 10 (11) (2018) 5280–5294.

[33] A. Roy, K.K. Gupta, S. Naskar, T. Mukhopadhyay, S. Dey, Compound influence of topological defects and heteroatomic inclusions on the mechanical properties of SWCNTs, Mater. Today Commun. 26 (2021), 102021.

[34] K.K. Gupta, L. Roy, S. Dey, Hybrid machine-learning-assisted stochastic nano-indentation behaviour of twisted bilayer graphene, J. Phys. Chem. Solid 167 (2022), 110711.

[35] T. Mukhopadhyay, A. Mahata, S. Naskar, S. Adhikari, Probing the Effective Young's Modulus of 'Magic Angle'Inspired Multi-Functional Twisted Nano-Heterostructures, Advanced Theory and Simulations 3 (10) (2020) 2000129.

[36] T. Mukhopadhyay, A. Mahata, S. Adhikari, M. Zaeem, Effective mechanical properties of multilayer nano-heterostructures, Sci. Rep. 7 (1) (2017) 1–13.

[37] X. Yang, B. Zhang, Twisted bilayer graphene/h-BN under impact of a nano-projectile, Appl. Surf. Sci. 538 (2021), 148030.

[38] H. Tian, B. Zhang, Q.M. Li, Ballistic response of hexagonal boron nitride monolayer under impact of a nano-projectile, Mech. Mater. 133 (2019) 1–12.

[39] K.K. Gupta, T. Mukhopadhyay, L. Roy, S. Dey, High-velocity ballistics of twisted bilayer graphene under stochastic disorder, Adv. Nano Res. 12 (5) (2022) 529–547.

[40] M.A.N. Dewapriya, R.E. Miller, Energy absorption mechanisms of nanoscopic multilayer structures under ballistic impact loading, Comput. Mater. Sci 195 (2021), 110504.

[41] G. Yang, X. Guo, G.J. Weng, L.L. Zhu, R. Ji, Simulation of ballistic performance of coarse-grained metals strengthened by nanotwinned regions, Model. Simul. Mater. Sci. Eng. 23 (8) (2015), 085009.

[42] M.A.N. Dewapriya, R.E. Miller, Molecular dynamics study of the penetration resistance of multilayer polymer/ceramic nanocomposites under supersonic projectile impacts, Extreme Mech. Lett. 44 (2021), 101238.

[43] M.A.N. Dewapriya, R.E. Miller, Superior dynamic penetration resistance of nanoscale multilayer polymer/metal films, J. Appl. Mech. 87 (12) (2020).

[44] M.A.N. Dewapriya, R.E. Miller, Molecular dynamics study of the mechanical behaviour of ultrathin polymer–metal multilayers under extreme dynamic conditions, Comput. Mater. Sci 184 (2020), 109951.

[45] H. Tian, B. Zhang, Nano-projectiles impact on graphene/SiC laminates, Appl. Surf. Sci. 591 (2022), 153113.

[46] S. Zhao, Y. Zhang, J. Yang, S. Kitipornchai, Folded graphene reinforced nanocomposites with superior strength and toughness: A molecular dynamics study, J. Mater. Sci. Technol. 120 (2022) 196–204.

[47] A. Agrawal, R. Mirzaeifar, Graphene-Nickel interaction in layered metal-matrix composites, Surf. Sci. 688 (2019) 1–6.

[48] Y. Rong, H.P. He, L. Zhang, N. Li, Y.C. Zhu, Molecular dynamics studies on the strengthening mechanism of Al matrix composites reinforced by grapnene nanoplatelets, Comput. Mater. Sci 153 (2018) 48–56.

[49] Y. Chandra, S. Adhikari, S. Mukherjee, T. Mukhopadhyay, Unfolding the mechanical properties of buckypaper composites: nano-to macro-scale coupled atomistic-continuum simulations, Eng. Comput. (2022) 1–31.

[50] F. Soto, A. Martin, S. Ibsen, M. Vaidyanathan, V. Garcia-Gradilla, Y. Levin, A. Escarpa, S.C. Esener, J. Wang, Acoustic microcannons: Toward advanced microballistics, ACS Nano 10 (1) (2016) 1522–1528.

[51] Y.C. Wu, J.L. Shao, H. Zhan, Damage and self-healing characteristics of monolayer graphene enhanced Cu under ballistic impact, Mech. Mater. 155 (2021), 103736.

[52] Z. Meng, S. Keten, Unraveling the effect of material properties and geometrical factors on ballistic penetration energy of nanoscale thin films, J. Appl. Mech. 85 (12) (2018), 121004.

[53] K. Momma, F. Izumi, VESTA: a three-dimensional visualization system for electronic and structural analysis, J. Appl. Cryst. 41 (3) (2008) 653–658.

[54] L. Martínez, R. Andrade, E.G. Birgin, J.M. Martínez, PACKMOL: a package for building initial configurations for molecular dynamics simulations, J. Comput. Chem. 30 (13) (2009) 2157–2164.

[55] W. Lee, S. Jang, M.J. Kim, J.M. Myoung, Interfacial interactions and dispersion relations in carbon–aluminium nanocomposite systems, Nanotechnology 19 (28) (2008), 285701.

[56] W.G. Jiang, Y. Wu, Q.H. Qin, D.S. Li, X.B. Liu, M.F. Fu, A molecular dynamics based cohesive zone model for predicting interfacial properties between graphene coating and aluminum, Comput. Mater. Sci 151 (2018) 117–123.

[57] Y. Mishin, D. Farkas, M.J. Mehl, D.A. Papaconstantopoulos, Interatomic potentials for monoatomic metals from experimental data and ab initio calculations, Phys. Rev. B 59 (5) (1999) 3393.

[58] T.C. O'Connor, J. Andzelm, M.O. Robbins, AIREBO-M: A reactive model for hydrocarbons at extreme pressures, J. Chem. Phys. 142 (2) (2015), 024903.

[59] B.Z.G. Haque, S.C. Chowdhury, J.W. Gillespie Jr, Molecular simulations of stress wave propagation and perforation of graphene sheets under transverse impact, Carbon 102 (2016) 126–140.

[60] A.P. Thompson, H.M. Aktulga, R. Berger, D.S. Bolintineanu, W.M. Brown, P.S. Crozier, P.J. in't Veld, A. Kohlmeyer, S.G. Moore, T.D. Nguyen, R. Shan, LAMMPS-a flexible simulation tool for particle-based materials modeling at the atomic, meso, and continuum scales, Comput. Phys. Commun., 271, p.108171, 2022.

[61] A. Stukowski, Visualization and analysis of atomistic simulation data with OVITO–the Open Visualization Tool, Model. Simul. Mater. Sci. Eng. 18 (1) (2009), 015012.

[62] J. Cai, R. Thevamaran, Superior energy dissipation by ultrathin semicrystalline polymer films under supersonic microprojectile impacts, Nano Lett. 20 (8) (2020) 5632–5638.

[63] J. Hyon, O. Lawal, O. Fried, R. Thevamaran, S. Yazdi, M. Zhou, D. Veysset, S. E. Kooi, Y. Jiao, M.S. Hsiao, J. Streit, Extreme energy absorption in glassy polymer thin films by supersonic micro-projectile impact, Mater. Today 21 (8) (2018) 817–824.

[64] Y. Chandra, T. Mukhopadhyay, S. Adhikari, F. Figiel, Size-dependent dynamic characteristics of graphene based multi-layer nano hetero-structures, Nanotechnology 31 (2020), 145705.